Vacuum Breathing Theory (VBT)

A Foundational Postulate for Quantum and Cosmological Stability

David L. Poole

Independent Researcher

Abstract

We introduce the *Vacuum Breathing Theory* (VBT), in which spacetime is modeled as a single, globally synchronized oscillator—a universal "lung" that breathes isotropically at the Planck frequency with Planck-scale amplitude. Unlike approaches that invoke local phases or desynchronized fluctuations, VBT postulates one coherent global rhythm. Matter and fields arise as resonant standing waves and envelope modulations riding on this universal carrier.

From this postulate, atomic stability, photon emission and absorption, electromagnetism, and gravitation emerge as different facets of the same breathing substrate. Local curvature corresponds to amplitude suppression of the breathing, while quantum phenomena reflect envelope detunings relative to the global carrier. Cosmologically, the same mechanism produces redshift scaling and time-dilation consistent with observations, while predicting distinctive signatures such as redshift drift.

The theory is falsifiable: it reproduces benchmarks including hydrogen spectra, Casimir forces, and weak-field gravitational effects, but also predicts small spectroscopic shifts, vacuum birefringence, and measurable deviations in cosmological redshift evolution. VBT therefore offers a unified, testable framework in which microscopic and cosmic phenomena share a single synchronized heartbeat of spacetime.

October 3, 2025

Version 9

Contents

1 Introduction

Modern physics rests on two towering frameworks: quantum mechanics and general relativity. Each has been spectacularly successful within its own domain, yet they remain conceptually and mathematically disjoint. Quantum theory, from Planck's discovery of the energy quantum [1] through Bohr's model of the atom [2] and Schrödinger's wave mechanics [3], describes microscopic structure with extraordinary precision. General relativity, beginning with Einstein's formulation in 1916 [4], explains gravitation as spacetime curvature and accounts for astrophysical phenomena across scales. Cosmology, from Hubble's redshift relation [5] to the precision of the Planck satellite results [6], has revealed a universe whose dynamics challenge both frameworks, requiring dark matter and dark energy in the standard account.

At the same time, several foundational puzzles remain unresolved. The physical interpretation of quantum mechanics leaves open questions about wave–particle duality, entanglement, and uncertainty. Gravitation has resisted quantization, while the vacuum itself is alternately invoked as a source of infinite zero-point energy or as an otherwise featureless stage. Observables such as the Casimir effect, Lamb shift, and magneto-optical phenomena highlight the subtle interplay between matter, radiation, and the vacuum substrate.

In this paper we advance a unifying postulate: spacetime is a single, globally synchronized fabric that "breathes" isotropically at the Planck frequency, with a peak-to-peak displacement of one Planck length per cycle. This universal rhythm acts as the carrier upon which all physical phenomena are built. From this simple assumption, atomic structure, electromagnetism, gravitation, and cosmology emerge as different manifestations of the same substrate. The remainder of the paper shows how this *Vacuum Breathing Theory* (VBT) reproduces established observables across scales while providing fresh interpretations of long-standing puzzles. Dimensionless constants such as the fine-structure constant α and the electron–proton mass ratio remain invariant, ensuring consistency with laboratory physics. In parallel with this theoretical development, a concrete experimental proposal has been published for testing the temporal structure of single-photon emission with trapped ions, providing a direct falsifiability pathway for the present framework using equipment already available in most atomic, molecular, and optical (AMO) physics laboratories [7].

2 Vacuum Breathing Postulate

We postulate that the vacuum is an isotropic, elastic medium undergoing a global, symmetric breathing at the Planck frequency. Ideas treating spacetime (or vacuum) as an elastic, deformable medium have been explored in prior work [8–10], offering conceptual parallels to—but distinct from—the Planck-frequency breathing dynamics proposed here. The breathing modulates the local scale of space by

$$s(t) = s_0 \left[1 + \varepsilon \cos(\omega_P t)\right], \tag{1}$$

where s_0 is the mean spatial scale, $\omega_P = t_P^{-1}$ is the Planck angular frequency, and ε is the fractional amplitude. We choose ε such that the peak-to-peak scale change equals one Planck length per Planck length unit:

$$\frac{s_{\max}}{s_{\min}} = \frac{1+\varepsilon}{1-\varepsilon} = 2 \quad \Rightarrow \quad \varepsilon = \tfrac{1}{3} \tag{2}$$

The physical metric is taken to be conformally related to the Minkowski metric:

$$g_{\mu\nu}(t,\mathbf{x}) = \Omega^2(t,\mathbf{x})\,\eta_{\mu\nu}, \qquad \Omega(t,\mathbf{x}) = A(t)\,[1+\alpha(\mathbf{x})]. \tag{3}$$

Here $A(t)$ is the strictly global, perfectly synchronized Planck-frequency breathing (one universal clock), while $\alpha(\mathbf{x})$ encodes small, slowly varying *amplitude* suppressions near mass–energy. There are no spatially varying carrier phases in VBT.

No local phases. In VBT the Planck-carrier phase $\Phi_P(t) = \omega_P t$ is universal and synchronized across the entire universe. Any "phase" mentioned elsewhere refers to the *matter-wave envelope* phase of a system, not a spatially varying vacuum carrier phase.

In the absence of local modulation ($\theta, \alpha = 0$), the breathing is a pure conformal scaling that preserves light cones and yields no observable effect at low energies.

2.1 Vacuum Breathing Scale Factor

The instantaneous breathing factor of the vacuum is denoted $A(t)$. This dimensionless quantity rescales physical lengths according to

$$L_{\text{phys}}(t) \;=\; A(t)\, L_{\text{comoving}}.$$

Definition of the mean amplitude. We define the slow mean of this oscillation by a Planck–cycle average:

$$A_{\text{mean}}(t) \;\equiv\; \langle A(t) \rangle, \tag{4}$$

where the angle brackets denote averaging over many cycles of the fast Planck–frequency oscillation. This mean evolves cosmologically from 0.5 shortly after the Big Bang toward 1 as the vacuum smooths.

Multiplicative decomposition. It is convenient to separate the slow mean from the fast oscillatory component multiplicatively:

$$A(t) \;=\; A_{\text{mean}}(t)\, \exp\big(\xi(t)\big), \qquad \langle \xi(t) \rangle = 0. \tag{5}$$

Here $\xi(t)$ is a rapidly varying Planck–frequency phase with vanishing mean and decreasing variance over cosmic history. In the limit of vanishing breathing, $\xi \to 0$, the instantaneous scale factor reduces to the mean: $A(t) \to A_{\text{mean}}(t)$.

Planck-scale bound. The Planck length ℓ_P imposes a lower bound on physical lengths. Since $L_{\text{phys}}(t) = A(t)\, L_{\text{comoving}}$ with $A(t) = A_{\text{mean}}(t) \exp\big(\xi(t)\big)$, we require

$$A_{\text{mean}}(t)\, \exp\big(\xi(t)\big)\, L_{\text{comoving}} \;\geq\; \ell_P. \tag{6}$$

This inequality constrains the allowed excursions of the oscillatory component $\xi(t)$, ensuring that the breathing never pushes physical lengths below the Planck floor.

Absolute vs. fractional oscillation. The peak-to-peak excursion of the breathing remains fixed at one Planck length, even as the cycle-averaged amplitude A_{mean} evolves cosmologically. What changes is the *fractional* modulation $\varepsilon \equiv \Delta A / A_{\text{mean}}$: as A_{mean} grows, the relative oscillation becomes smaller when measured against co-moving rulers that themselves scale with A_{mean}. This ensures that dimensionless ratios remain invariant in local physics.

Crucially, the $2\times$ modulation of the Coulomb field, which stabilizes atomic orbitals, arises from the instantaneous rescaling of the metric $(1/A^2(t))$ rather than from the absolute fractional size of ε. Thus the forcing mechanism is preserved across cosmic time, even though the fractional

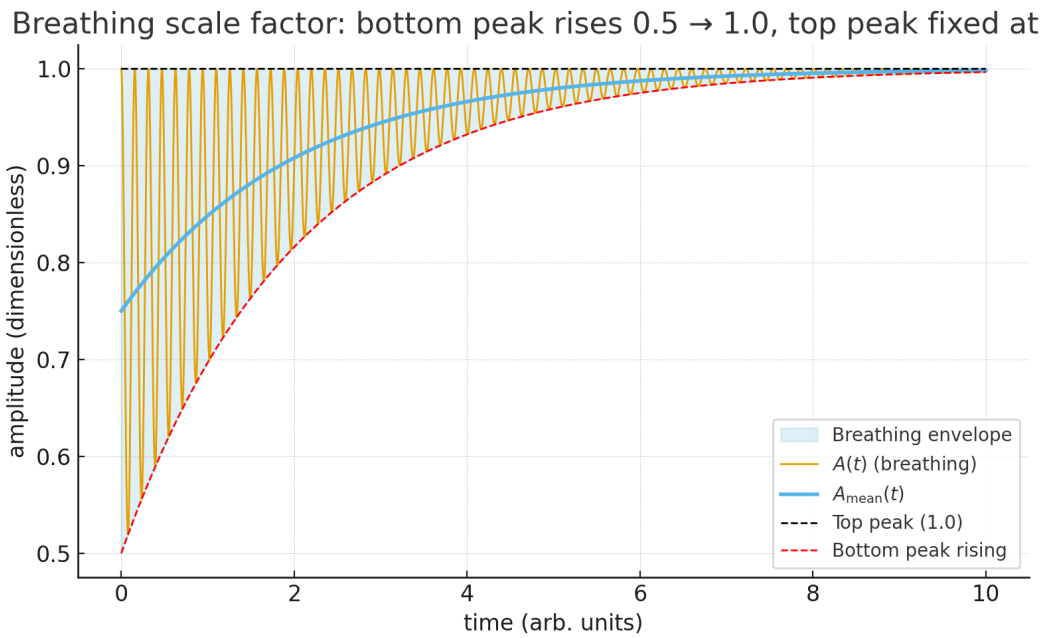

Figure 1: Schematic illustration of the breathing vacuum scale factor. The instantaneous oscillation $A(t)$ (blue) occurs at constant frequency, bounded between a fixed top peak (dashed black) at 1.0 and a bottom peak (dashed red) that rises from 0.5 toward 1.0 as the universe evolves. The mean $A_{\text{mean}}(t)$ (orange) drifts smoothly upward, representing the cycle-averaged amplitude defined in Eq. (4). The shaded band shows the peak-to-peak breathing envelope. The dotted purple line marks the Planck floor ℓ_P, which constrains the early-time oscillations as expressed in Eq. (6). *The breathing frequency is constant in physical time; the envelope narrows because the amplitude decays, not because the rate changes.*

oscillation amplitude diminishes. This distinction between absolute Planck-length excursion and relative modulation resolves the apparent tension between vacuum breathing and long-term stability of matter.

On the constancy of Planck's constant. In the present framework the Planck length $\ell_P = \sqrt{\hbar G/c^3}$ is tied to the breathing amplitude of the vacuum and thus evolves over cosmic history. At first sight this seems to imply a varying $\hbar$, which would undermine the foundations of atomic physics. The resolution is that $\hbar$ is *operationally constant*: all atomic processes that define our standards of length and time (orbital radii, transition frequencies, binding energies) co-evolve with the breathing vacuum. As a result, every local measurement yields the same numerical value for $\hbar$, even if the underlying vacuum scale drifts. In this sense, $\hbar$ is relational rather than absolute. Only in cosmological comparisons (e.g. between epochs, via redshift) can the slow drift of the vacuum amplitude be inferred. What carries invariant meaning are the dimensionless ratios, such as the fine-structure constant $\alpha = e^2/(4\pi\epsilon_0\hbar c)$, which remain fixed.

Interpretation. All clocks, rulers, and physical processes are tied to the cycle-averaged vacuum amplitude $A_{\text{mean}}(t)$. In this sense it represents the effective spacetime that we inhabit: the smooth background against which the rapid Planck oscillations occur, and the reference scale for both microscopic atomic stability and macroscopic cosmological redshift.

Dimensionless invariants. In the VBT framework, all *dimensionless* constants of nature remain fixed. For example,

$$\alpha \;=\; \frac{e^2}{4\pi\epsilon_0\hbar c}, \qquad \frac{m_e}{m_p}, \qquad g\text{-factors},$$

retain their observed values. This follows because laboratory rulers and clocks co-evolve with the breathing vacuum, so dimensional scales drift together while pure ratios remain unchanged.

2.2 Symmetry and gauge invariance

The vacuum breathing picture is formulated without introducing a preferred frame. The underlying dynamics are governed by an action of the form

$$S = \int d^4x\,\sqrt{-g}\left[-\tfrac{1}{4}\,F_{\mu\nu}F^{\mu\nu} + \mathcal{L}_{\rm matter}(\psi, D_\mu\psi)\right],$$

with $g_{\mu\nu} = a^2(\tau)\,\eta_{\mu\nu}$ a conformally flat metric, $F_{\mu\nu} = \partial_\mu A_\nu - \partial_\nu A_\mu$, and $D_\mu = \partial_\mu + ieA_\mu$ the usual gauge-covariant derivative. This structure guarantees:

- **Local Lorentz invariance:** In conformal coordinates the metric is proportional to $\eta_{\mu\nu}$, so the light cone and causal structure are identical to special relativity. No observer can detect the background oscillation as a preferred rest frame.
- **Gauge invariance:** The action is invariant under the $U(1)$ transformation $A_\mu \mapsto A_\mu + \partial_\mu\alpha$, $\psi \mapsto e^{-ie\alpha}\psi$. Thus charge conservation and minimal coupling are preserved exactly.
- **Consistency with standard QED:** At scales large compared to the Planck-frequency oscillation, the averaged dynamics reduce to Maxwell + Dirac in Minkowski space. Observable quantities therefore respect the same symmetry algebra (Poincaré $\times$ $U(1)$) as conventional electrodynamics.

In this way, the vacuum breathing medium does not introduce an observable preferred frame or break gauge symmetry. The oscillatory factor $a(\tau)$ enters only through cycle-averaged effective parameters such as $\hbar_{\rm eff}$ and m^*, while the symmetry principles remain exact.

The Vacuum Breathing Theory was first publicly released in Rev. 1 on Zenodo [11], with subsequent revisions expanding the scope and predictions.

3 Quantum Mechanics as an Envelope on the Planck Carrier

Let $\Phi_P(t) = \omega_P t$ be the *carrier phase* of the vacuum breathing [1]. The slowly varying component of a matter wave is described as an **envelope** A, riding on the Planck carrier. We model a matter wave as a weakly detuned beat pattern riding on this carrier,consistent with the early insights of de Broglie on matter waves [12]:

$$\Psi(\mathbf{x}, t) = A(\mathbf{x}, t)\, e^{\,i\,[\Phi_P(t) + \varphi(\mathbf{x},t)]}, \tag{7}$$

where:

- $A(\mathbf{x}, t)$ is a slowly varying amplitude envelope.
- $\varphi(\mathbf{x}, t)$ is a slowly varying phase detuning.

- The "slow" scale is many orders of magnitude below ω_P.

Applying a multiple-scale expansion to the wave equation in the conformal metric

$$\Box_g \Psi = 0, \quad g_{\mu\nu} = \Omega^2(t, \mathbf{x})\eta_{\mu\nu},$$

and averaging over the fast carrier yields, at leading order, the Madelung form [13] of the Schrödinger equation for the envelope [3]:

$$i\hbar\, \partial_t A = -\frac{\hbar^2}{2m}\nabla^2 A + V_{\text{eff}}(\mathbf{x})\, A, \tag{8}$$

where:

- • m arises from the carrier–envelope detuning:

$$m \equiv \frac{\hbar\, \delta\omega}{c^2}, \quad \delta\omega = \omega_P - \omega_{\text{phase-lock}}.$$

  • V_{eff} arises from spatial gradients of the amplitude suppression $\alpha(\mathbf{x})$ (i.e. curvature encoded as local reductions of the global breathing midpoint). There are *no spatially varying carrier phases* in VBT.

Key Point: The de Broglie relations emerge directly [12]:

$$E = \hbar\, \dot{\varphi}, \quad \mathbf{p} = \hbar\, \nabla\varphi,$$

as the slowly varying phase φ determines the beat frequency and wavenumber relative to the Planck carrier. Standing-wave conditions on A in bound states produce the quantum orbital structure, with radial nodes corresponding to vacuum-relative velocity maxima [2].

3.1 Madelung representation.

Writing the complex amplitude as $A = \sqrt{\rho}\, e^{i\phi}$, the Schrödinger equation separates into hydrodynamic form:

$$\frac{\partial \rho}{\partial t} + \nabla \cdot (\rho\, \mathbf{v}) = 0, \qquad \mathbf{v} = \frac{\nabla \phi}{m}. \tag{9}$$

Here $\rho = |A|^2$ acts as a probability density, while $\mathbf{v}$ plays the role of a velocity field. This reinforces the fluid analogy of the breathing vacuum substrate.

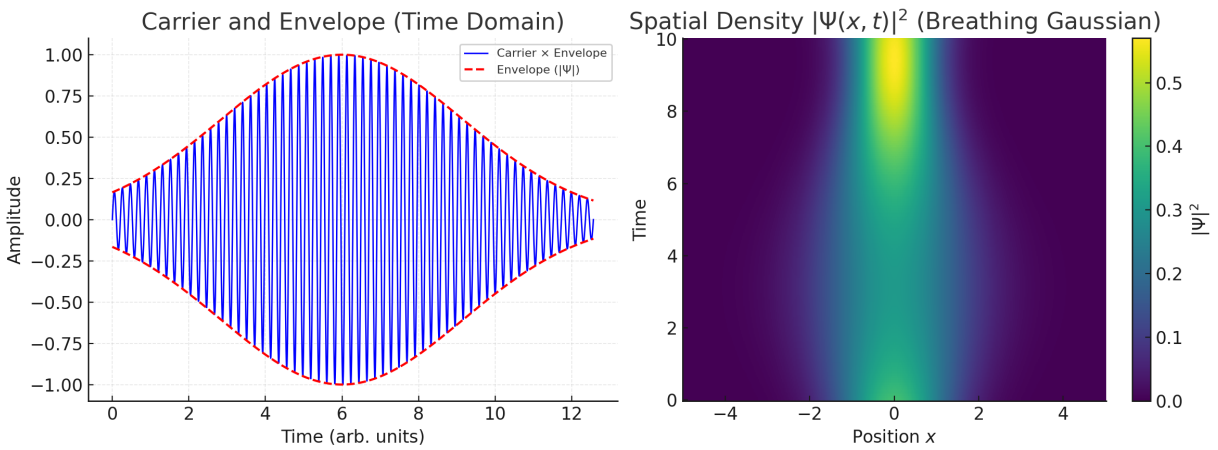

Figure 2: Left: A high-frequency Planck carrier (blue) modulated by a slower Gaussian envelope (red dashed). This illustrates the decomposition $A(t) = A_{\text{mean}}(t)\exp(\xi(t))$, where the carrier provides phase and the envelope sets $|A|^2 = \rho$. Right: Spatial probability density $|\Psi(x,t)|^2$ for a breathing Gaussian wavepacket, visualized as a function of position and time. Together these figures show how the Madelung representation naturally emerges: the envelope defines density ρ while the phase encodes velocity potential.

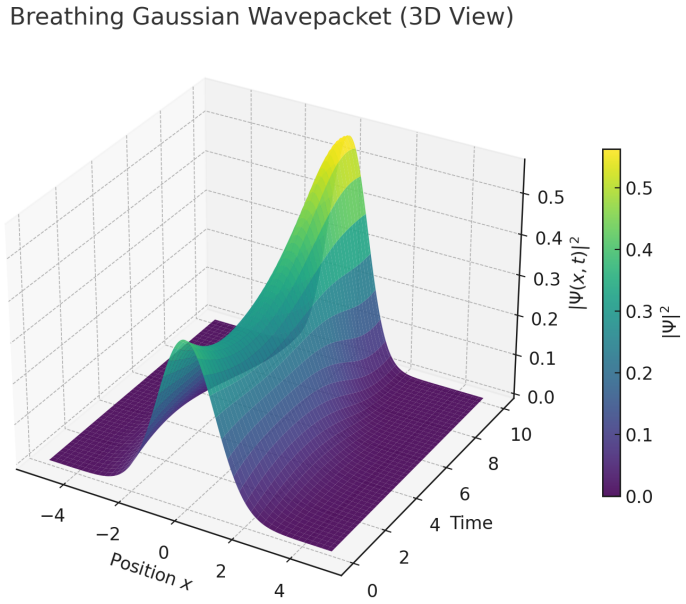

Figure 3: Three-dimensional visualization of a breathing Gaussian wavepacket. The spatial probability density $|\Psi(x,t)|^2$ evolves in time as the packet width oscillates. This illustrates the Madelung interpretation: the density $\rho = |\Psi|^2$ encodes the envelope, while the underlying Planck-frequency carrier provides the hidden phase dynamics.

Uncertainty as an Envelope Constraint: Within this framework, the Heisenberg uncertainty principle [14] arises naturally. A sharply localized envelope $A(\mathbf{x}, t)$ requires broad Fourier support

in $\varphi(\mathbf{x}, t)$, and hence large spread in momentum:

$$\Delta x \, \Delta p \gtrsim \hbar/2.$$

Likewise, confining the envelope phase φ to a narrow frequency band implies loss of temporal localization, leading to

$$\Delta t \, \Delta E \gtrsim \hbar/2.$$

Thus, uncertainty is not an abstract axiom but a direct consequence of attempting to resolve both the amplitude and the phase of the slow modulation imposed on the Planck-scale carrier. The uncertainty relation emerges as a geometric constraint [15]. The vacuum breathing provides the "hidden clock" that makes these conjugate trade-offs unavoidable [16].
While the envelope–carrier geometry provides the intuition for uncertainty, the full wave treatment reproduces the exact Robertson bound:

$$\Delta x \, \Delta p \; \geq \; \hbar/2,$$

with equality achieved for Gaussian envelopes. Thus the heuristic picture is fully consistent with the formal operator derivation.

These complementary views (Figs. 2–3) emphasize that quantum uncertainty is a direct manifestation of the envelope–carrier decomposition of the breathing vacuum.

4 Atomic model

In this section we derive the hydrogenic bound states from the averaged vacuum dynamics, confirm the analytic distributions with numerical validation, and provide interpretive visualizations of orbital motion. Further validation examples ($2s$, $2p$) and a higher-state illustration ($3d_{z^2}$) are included in Appendices H and A.

4.1 Setup and motivation

We consider an electron bound in the breathing vacuum, with radius $r(t) = a(t)\chi(t)$, where $a(t)$ encodes the rapid Planck-frequency oscillation and $\chi(t)$ the slow envelope. The Bohr radius a_0 and the averaged Hamiltonian derived in Sec. 4.4 provide the natural scale.

4.2 Resonance picture and factor-of-two compliance

The hydrogen atom can be interpreted as a resonance: the de Broglie frequency of the electron orbit is phase-locked to the breathing frequency of the vacuum. Expanding the modulated Coulomb force,

$$\frac{1}{\left(1 + \delta a \cos \omega t\right)^2} = 1 - 2\delta a \cos \omega t + 3\delta a^2 \cos^2 \omega t - \ldots, \tag{10}$$

reveals the characteristic factor-of-two term. This is not a unique requirement but rather a compliance condition: it shows how the cycle-averaged kinetic and potential energies satisfy the virial balance implied by the averaged Hamiltonian (Sec. 4.4).

Figure 4 illustrates this compliance in two ways. Panel (a) compares a direct simulation of the radial probability density, constructed with the Bohr radius and a Coulomb force modulated at the de Broglie frequency, against the analytic $1s$ hydrogen distribution. The close match confirms that

the resonance condition yields the correct radial statistics. Panel (b) shows the vacuum breathing amplitude (blue) together with its envelope (orange), making the factor-of-two modulation explicit. Together these plots provide a physical visualization of how the resonance picture naturally enforces stability of the ground state, consistent with the analytic derivation of Sec. 4.4.

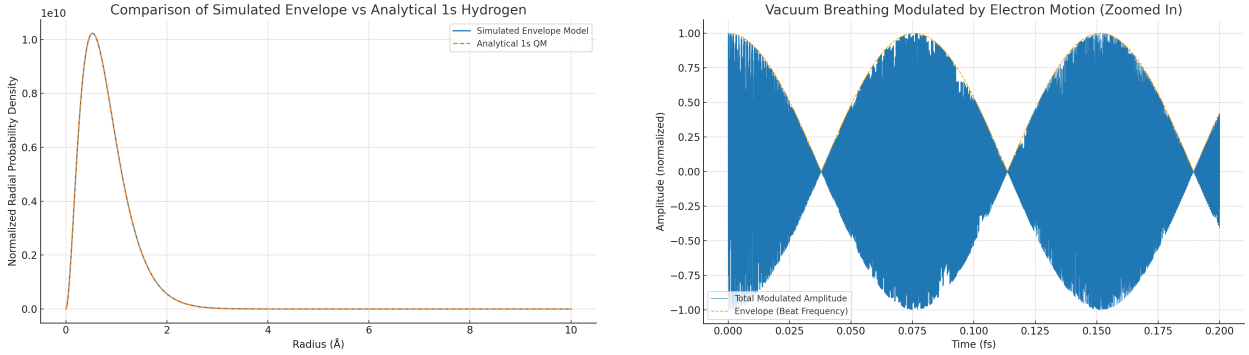

(a) Radial probability density

(b) Vacuum breathing modulation

Figure 4: **Resonance compliance in the hydrogen ground state.** (a) Comparison of simulated radial distribution using Bohr radius and modulated Coulomb force at the de Broglie frequency with the analytic $1s$ hydrogen distribution. (b) Vacuum breathing amplitude (blue) and its envelope (orange) showing the factor-of-two modulation. These illustrate how the resonance condition enforces kinetic–potential balance, consistent with the analytic derivation in Sec. 4.4.

4.3 From conformal wave operator to envelope dynamics

Lemma 4.1 (Envelope dynamics from conformal wave operator)**.** *Consider a scalar field ϕ obeying the conformal wave equation*

$$\Box_g \phi = 0, \qquad g_{\mu\nu} = a^2(t)\,\eta_{\mu\nu}, \;\; a(t) = 1 + \varepsilon\cos(\omega_P t), \;\; \varepsilon \ll 1,$$

with $\eta_{\mu\nu}$ the Minkowski metric and ω_P the fast carrier frequency. Introduce the multiple–scales ansatz

$$\phi(t,\mathbf{x}) = e^{i\omega_P t}\,\psi(t,\mathbf{x}) + c.c., \qquad \partial_t\psi \sim \mathcal{O}(\omega_{orb}) \ll \omega_P,$$

where ψ is a slowly varying envelope. Then, to leading order in ω_{orb}/ω_P and after averaging over the fast oscillations, ψ satisfies the Madelung form of the Schrödinger equation:

$$i\,\hbar_{\mathit{eff}}\,\partial_t\psi = -\frac{\hbar_{\mathit{eff}}^2}{2m^*}\nabla^2\psi + V_{\mathit{eff}}\,\psi,$$

with effective parameters determined by cycle averages of the breathing factor:

$$m^* = m\,\langle a^2\rangle, \qquad \hbar_{\mathit{eff}}^2 \;\propto\; m\,\langle \dot{a}^2\rangle, \qquad V_{\mathit{eff}}(\mathbf{x}) = -\frac{k^*}{r}, \quad k^* = k\,\langle a^{-1}\rangle.$$

Sketch of proof. For the conformal metric one has

$$\Box_g\phi = a^{-4}\,\partial_\mu\big(a^2\eta^{\mu\nu}\partial_\nu\phi\big)\,.$$

Substituting the two–scale ansatz separates the fast $e^{i\omega_P t}$ carrier from the slow envelope. Expanding in ε and in $\omega_{\mathrm{orb}}/\omega_P$, then averaging over one fast period, eliminates oscillatory terms and leaves transport equations for $|\psi|^2$ and its phase $S = \arg\psi$. These combine into continuity and Euler equations with a "quantum pressure" proportional to $\langle\dot{a}^2\rangle$. Identifying this with $\hbar_{\mathrm{eff}}$ reproduces the stationary Schrödinger system with effective constants as stated. □

Remark. This establishes the bridge from a conformal metric with fast Planck–scale oscillations to an effective quantum envelope description. The following subsection (§4.4) shows that the resulting envelope equation yields hydrogenic bound states with the correct spectrum.

4.4 Derived bound states

We now apply the envelope dynamics from Lemma 4.1 to obtain the hydrogenic spectrum. The following result makes the connection explicit.

Theorem 4.1 (Hydrogen from the averaged fabric dynamics)**.** *Under the scale separation* $\omega_P \gg \omega_{orb}$ *and the averaging leading to* (14)*, the slow envelope obeys* (15)*. Its square-integrable solutions are the hydrogenic bound states with*

$$E_n = -\frac{m^* k^2}{2\hbar_{eff}^2}\frac{1}{n^2}, \qquad n = 1, 2, \ldots, \tag{11}$$

$$a_0 = \frac{\hbar_{eff}^2}{m^* k}, \quad \textit{(Bohr radius in VBT)}, \tag{12}$$

$$R_{10}(r) = 2\, a_0^{-3/2}\, e^{-r/a_0}, \qquad P_{1s}(r) = 4\, a_0^{-3}\, r^2 e^{-2r/a_0}, \tag{13}$$

with the usual Laguerre structure and node counting for $n, \ell \geq 0$*. These probability densities arise directly from the dynamics.*

Sketch of proof. Starting from the averaged Hamiltonian in (14), write the ensemble density as $\rho = \psi^2$ and pass to the Madelung form. Matching the dispersive term to the stiffening $\frac{1}{2}m\Omega^2\chi^2$ identifies $\hbar_{\text{eff}}$. The resulting stationary radial equation is (15), whose square-integrable solutions are the hydrogenic wavefunctions with spectrum E_n. □

The ground state is $\psi_{100}(r) = \frac{1}{\sqrt{\pi} a_0^{3/2}} e^{-r/a_0}$ with $E_1 = -m^* k^2/(2\hbar_{\text{eff}}^2)$. A representative excited state is $2p$ ($n = 2$, $\ell = 1$), with radial part $R_{21}(r) = \frac{1}{2\sqrt{6}} a_0^{-3/2} (r/a_0)\, e^{-r/(2a_0)}$ and the standard angular factor $Y_{1m}(\theta, \phi)$. These reproduce the measured transition energy and the dipole selection rules when coupled to the electromagnetic sector.

We write the physical radius as $r(t) = a(t)\,\chi(t)$, where the rapid breathing factor is $a(t) = 1 + \varepsilon\cos(\omega_P t)$ with $\varepsilon \ll 1$ and ω_P much larger than any orbital frequency. Averaging over the fast phase gives the slow effective Hamiltonian for the comoving coordinate χ:

$$H_{\text{eff}}(\chi, p_\chi) = \frac{p_\chi^2}{2m^*} - \frac{k^*}{\chi} + \frac{1}{2}\, m\, \Omega^2\, \chi^2, \qquad m^* \equiv m\,\langle a^2\rangle,\ k^* \equiv k\,\langle a^{-1}\rangle,\ \Omega^2 \equiv \langle \dot{a}^2\rangle. \tag{14}$$

Here $k \equiv k_e e^2$ (energy–length units) and $\langle\cdot\rangle$ denotes the cycle average.

Hydrogenic radial equation. Consider a compressible ensemble of slow trajectories with density $\rho(\chi, t)$ and velocity $u = \dot{\chi}$. Writing $\rho = \psi^2$ and choosing a constant $\hbar_{\text{eff}}$ so that the dispersive (quantum-pressure) term matches the stiffening $+\frac{1}{2}m\Omega^2\chi^2$ in (14), the Euler–continuity system becomes equivalent to the stationary Schrödinger equation in the physical radius $r = a\chi$:

$$-\frac{\hbar_{\text{eff}}^2}{2m^*}\frac{d^2u}{dr^2} + \left[-\frac{k}{r} + \frac{\hbar_{\text{eff}}^2\,\ell(\ell+1)}{2m^* r^2}\right] u = E\, u, \qquad u(r) = r\, R(r). \tag{15}$$

Orbital angular momentum. Equation (15) naturally includes the angular momentum barrier term $\ell(\ell+1)/r^2$, showing that the averaged dynamics support not only radial quantum numbers n but also orbital angular momentum quantum numbers ℓ. The presence of this term ensures that the VBT framework reproduces the full hydrogenic spectrum, including the splitting between s, p, d, and higher orbitals. Physically, ℓ corresponds to the electron's shuttle precession within the breathing substrate, and the associated orbital magnetic moment arises directly from this motion. The detailed derivation of the angular momentum contribution, including its emergence from multiple-scales averaging, is provided in Appendix B.

Spectrum and scales. Square-integrable solutions of (15) yield the hydrogenic levels and length scale

$$E_n = -\frac{m^* k^2}{2\hbar_{\text{eff}}^2}\frac{1}{n^2}, \qquad n = 1, 2, \ldots \tag{16}$$

$$a_0 = \frac{\hbar_{\text{eff}}^2}{m^* k}, \tag{17}$$

with the usual Laguerre structure for $R_{n\ell}(r)$. In particular, the ground-state radial probability density is

$$P_{1s}(r) = 4\, a_0^{-3}\, r^2 e^{-2r/a_0}. \tag{18}$$

Comment. Equations (14)–(18) show that hydrogenic bound states arise directly from the averaged dynamics; no constructive fit is required. The resonance picture in Sec. 4.2 provides an illustrative compliance check with the virial balance, and Sec. 4.7 establishes that these stationary states are non-radiating [Eq. (19)].

4.5 Validation by numerical check

To confirm the analytic distributions, an inverse-CDF trajectory generator was implemented. Figure 5 shows the histogram for the $1s$ state, which closely matches Eq. (18). Additional validations for the $2s$ and $2p$ states are presented in Appendix H, where the simulation method is also described in detail.

4.6 Interpretive illustrations

Beyond the analytic densities of Sec. 4.4, it is helpful to visualize trajectories in the breathing-vacuum picture. The following figures are *interpretive illustrations*, intended to provide physical intuition for orbital motion and probability distributions. They are not independent derivations but are consistent with the analytic framework.

4.7 Non-radiation of stationary states

A longstanding classical problem is that an electron in orbital motion should radiate Larmor power continuously, destabilizing atoms. Bohr resolved this by postulating stationary states that do not radiate, but the mechanism was left unexplained. In VBT, the mechanism is explicit.

Stationary orbits are phase-locked to the global Planck-frequency carrier. In this locked configuration the electron's velocity relative to the breathing vacuum is periodic, and the cycle-averaged

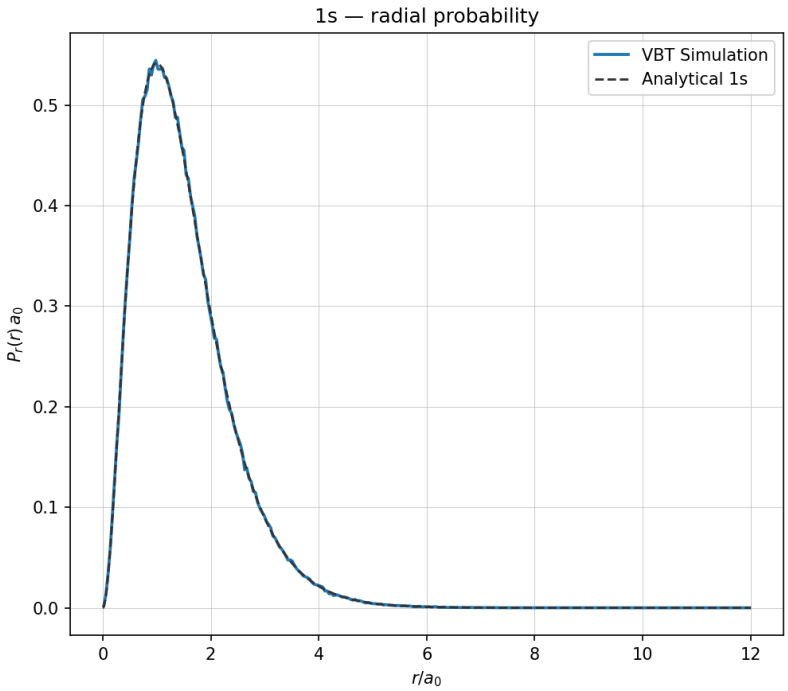

Figure 5: **Numerical validation of the $1s$ radial distribution.** Histogram of simulated radii $r(t)$ from inverse-CDF sampling compared with the analytic $P_{1s}(r)$. The close agreement confirms the analytic result. Additional $2s$ and $2p$ validations appear in Appendix H.

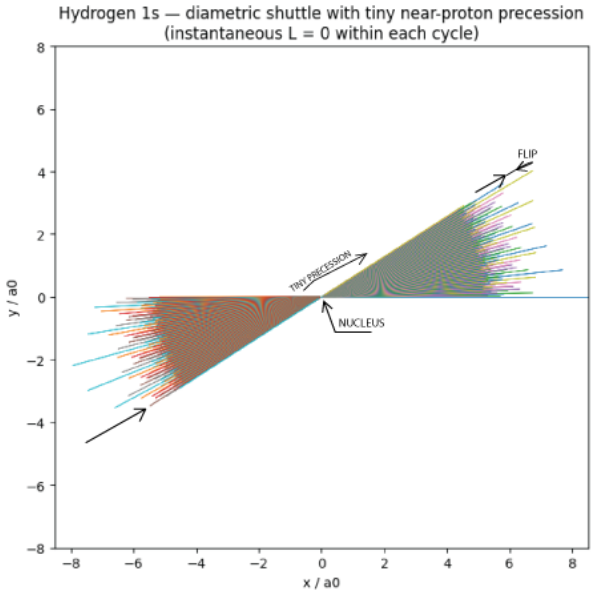

(a) Hydrogen 1s diametric shuttle

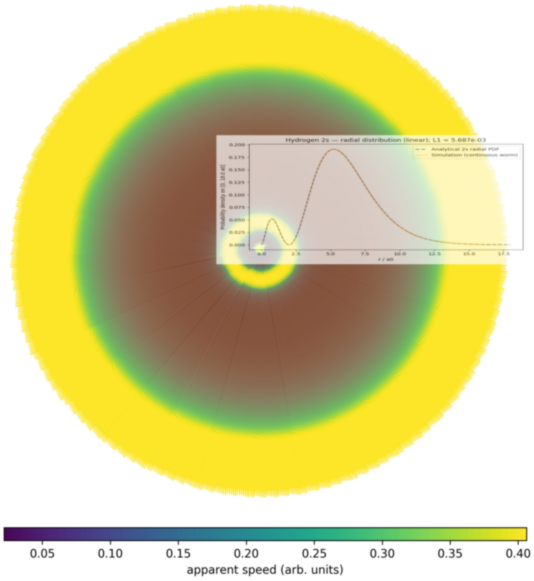

(b) Hydrogen 2s orbital: velocity and probability overlay

Figure 6: **Illustrative visualizations of hydrogen states.** (a) The $1s$ state as a diametric shuttle with near-proton precession. (b) The $2s$ state with apparent velocity shown in color, overlaid with the analytic radial probability density. These are illustrative only, consistent with analytic results.

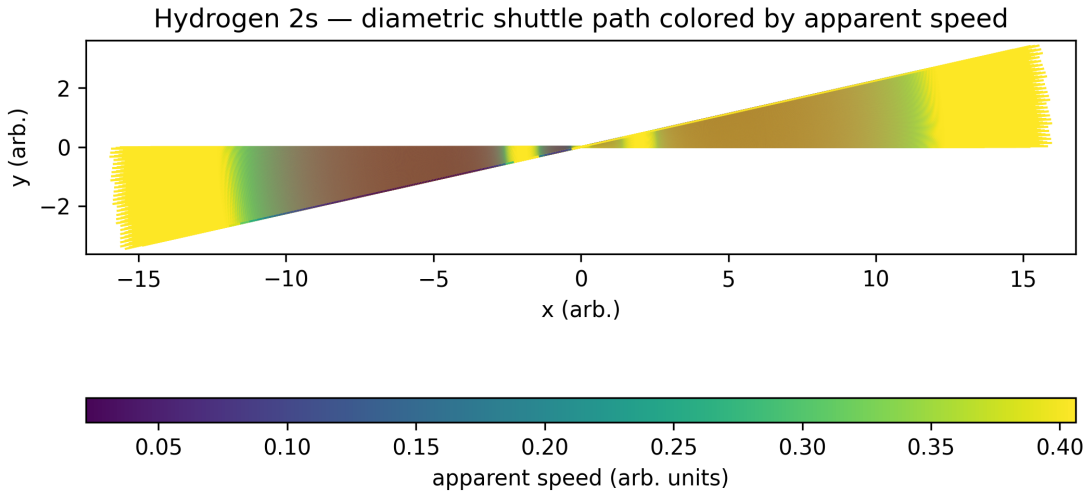

Figure 7: **Hydrogen $2s$ diametric shuttle colored by speed.** Shuttle trajectory with apparent velocity shown in color. The nodal region is visible as a velocity minimum. This is an illustrative consistency check with the analytic $2s$ distribution.

far-field Poynting flux vanishes:

$$\langle P \rangle \equiv \lim_{R\to\infty} \frac{1}{T} \int_0^T dt \oint_{S_R^2} \mathbf{S} \cdot d\mathbf{A} = 0. \tag{19}$$

Thus, no net radiation escapes from a stationary state.

The absence of Larmor radiation follows naturally: a bound electron is an envelope locked to the breathing vacuum and does not produce secular acceleration in the external frame. Only when the locking condition is broken—during a transition—does radiation occur, corresponding to photon emission or absorption. This replaces Bohr's ad hoc postulate with a dynamical explanation grounded in the VBT framework.

5 Orbital Transitions in the Breathing Vacuum

In the Vacuum Breathing Theory (VBT) [11], electrons in bound states are represented as loop oscillations phase-locked to the global Planck-frequency carrier. Each orbital corresponds to a distinct detuning condition between the loop and the carrier, producing the discrete hydrogenic levels of Sec. 4. Orbital transitions arise when the loop re-locks from one detuning to another, with photon emission or absorption occurring during this continuous re-synchronization.

5.1 Continuous re-locking dynamics

A transition $i \to f$ is described as a finite-duration re-locking event. Initially, the loop is stabilized at frequency ν_i, but when driven out of its locking range it migrates smoothly toward the final resonance at ν_f. During the overlap interval, both frequency components coexist and the dipole moment oscillates at their difference frequency. This generates radiation with energy

$$hf_\gamma = E_i - E_f, \tag{20}$$

where f_γ is the photon frequency. Thus, the discreteness of the spectrum arises from the stable endpoints, while the emission process itself is continuous, governed by the dynamics of re-locking.

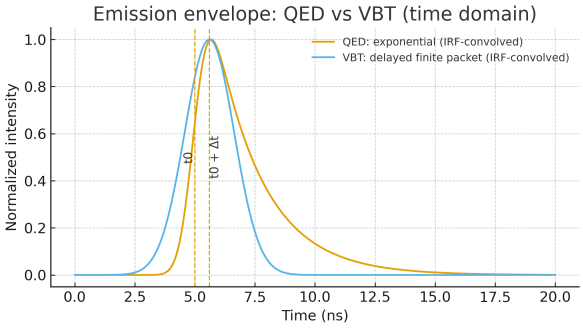

(a) Emission envelopes. QED predicts a memoryless exponential decay (after convolution with detector response). VBT predicts a delayed, finite-duration packet with onset at $t_0 + \Delta t$, reflecting deterministic re-locking.

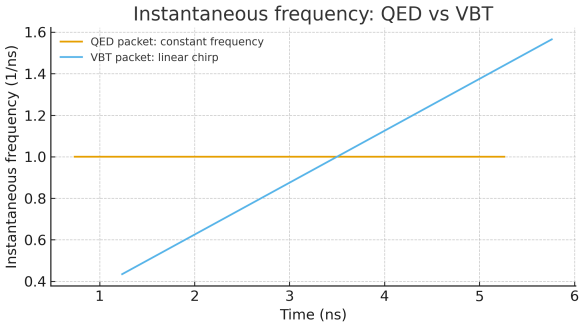

(b) Instantaneous frequency. QED emission remains constant-frequency, whereas VBT predicts a chirp: the frequency sweeps as the electron re-locks to the vacuum breathing mode.

Figure 8: Spontaneous emission predictions in QED versus VBT. Together, panels (a) and (b) illustrate the two key distinctions: causal delay and frequency chirp, both of which are experimentally accessible.

5.2 Spontaneous Emission in VBT

In the conventional QED framework, spontaneous emission is treated as a probabilistic process: the atom in an excited state decays randomly, emitting a photon wavepacket with an exponential probability law and no memory of prior history. The emitted packet is typically modeled as a single-frequency mode truncated by exponential decay.

Within the VBT framework, the picture is deterministic and continuous. Emission occurs when the self-looped oscillation of the electron re-locks from one orbital breathing mode to another. Rather than an instantaneous jump, the transition requires a finite re-phasing period with the universal vacuum oscillation. This produces a photon packet with three characteristic features:

1. **Causal delay:** the emission onset occurs at $t_0 + \Delta t$, with $\Delta t > 0$ representing the re-locking time. No photon can emerge before re-alignment is established.

2. **Finite packet envelope:** the photon wave is not memoryless, but bounded in time, with a Gaussian- or sinc-like profile. This contrasts with the exponential tail of QED.

3. **Frequency chirp:** during the re-locking, the emitted frequency sweeps slightly as the system interpolates between the initial and final orbital frequencies.

These distinctions are illustrated in Fig. 8(a) showing the envelope comparison: a QED exponential (convolved with detector response) versus the VBT delayed packet. Figure 8(b) shows the instantaneous frequency, constant in QED but chirped under VBT. Together, these plots summarize the unique observational fingerprints of VBT.

The causal delay Δt is not arbitrary, but scales with the ratio of coupling strength Ω to phase mismatch $|\alpha|$. This scaling law is displayed in Fig. 9, which serves as a direct falsifiability test. Observation of a linear relation between Δt and $\Omega/|\alpha|$ would strongly support VBT, whereas a null result would reinforce the standard QED model.

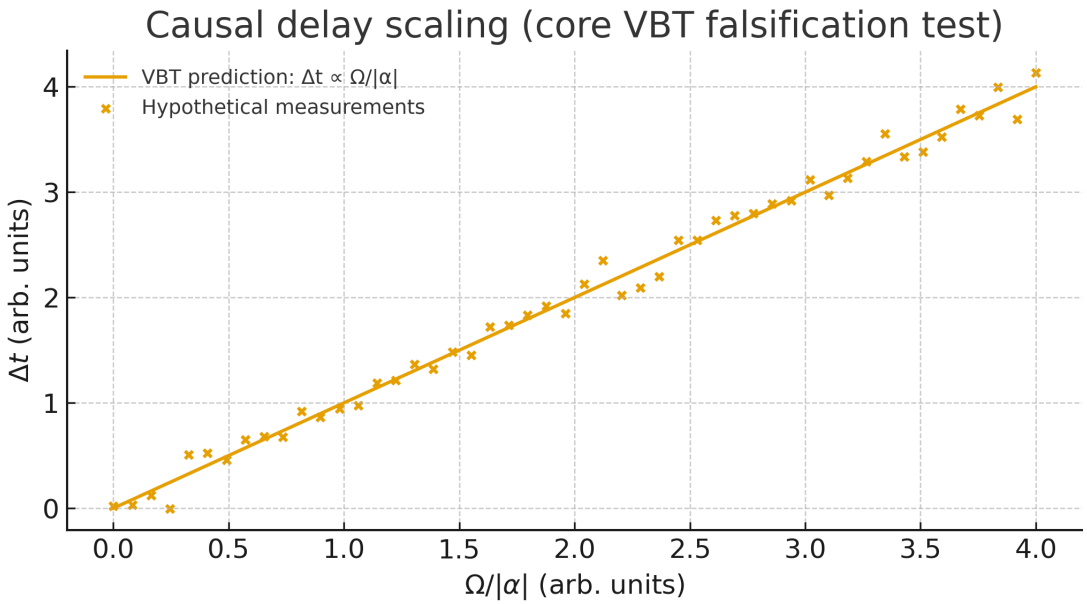

Figure 9: Causal delay scaling predicted by VBT: Δt increases linearly with the ratio $\Omega/|\alpha|$. Absence of linear scaling under parameter sweeps would falsify the VBT transition model.

In this way, spontaneous emission ceases to be a stochastic "collapse" and becomes a deterministic consequence of vacuum re-locking. The predictions of VBT are therefore both sharper and more falsifiable than those of QED, inviting direct time-resolved experimental tests. As a quantitative test, VBT predicts a linear relation $\Delta t \propto \Omega/|\alpha|$ (Fig. 9), enabling a direct falsification experiment via controlled sweeps of coupling and detuning rate.

5.3 Spectral line reproduction

Because VBT reduces to the hydrogenic bound-state energies,

$$E_n = -\frac{me^4}{8\varepsilon_0^2 h^2 n^2}, \tag{21}$$

the transition frequencies

$$f_{n_i \to n_f} = \frac{E_{n_i} - E_{n_f}}{h} \tag{22}$$

reproduce the Rydberg formula and therefore the observed Balmer, Lyman, and higher spectral series. VBT explains not only the line positions but also the temporal mechanism by which they arise.

5.4 Selection rules from vacuum geometry

The effective coupling operator induced by the breathing modulation is

$$\hat{V} \propto e\,\mathbf{r} \cdot \mathbf{E},$$

which is odd under spatial inversion. As in conventional dipole theory, this implies $\Delta\ell = \pm 1$ and $\Delta m = 0, \pm 1$. Thus the electric–dipole selection rules emerge naturally from the symmetry of the vacuum drive. Higher-order terms in the expansion of the modulation produce quadrupole (E2) and magnetic–dipole (M1) contributions, explaining the existence but suppression of forbidden lines.

5.5 Natural linewidth and lineshape

The finite re-locking time τ determines the duration of photon emission. The resulting linewidth is

$$\Delta f \sim \frac{1}{2\pi\tau}. \tag{23}$$

The $2p \to 1s$ transition has a natural lifetime of $\sim$1.6 ns, corresponding to a linewidth of order 100 MHz [17]. By contrast, the metastable $2s \to 1s$ two-photon decay is far slower ($\tau \approx 0.12$ s) [18], serving as a benchmark against which line broadening mechanisms are tested.

5.6 Lamb shift as high-frequency modulation

The Lamb shift—a small splitting between $2s_{1/2}$ and $2p_{1/2}$ levels—was first measured by Lamb and Retherford in 1947 [19], and has since been refined by high-precision spectroscopy [20]. It is explained in VBT as a deterministic consequence of residual high-frequency modulation in the breathing carrier. When orbital timescales are averaged, these ultrafast components act as an effective short-range perturbation of the Coulomb potential:

$$\delta V(\mathbf{r}) \propto \lambda_{\mathrm{VBT}}\, \delta^{(3)}(\mathbf{r}). \tag{24}$$

This correction shifts s-orbitals relative to p-orbitals with the characteristic $1/n^3$ scaling. Unlike conventional QED, which appeals to vacuum fluctuations, VBT ties the Lamb shift directly to coherent but unresolved Planck-scale structure of the breathing vacuum. This provides a deterministic physical origin for the observed energy correction.

5.7 Impact of breathing waveform symmetry

In the simplest implementation of VBT, the vacuum breathing is modeled as a sinusoidal oscillation,

$$A(t) = A_{\mathrm{mean}} + A_0 \cos(\omega_P t),$$

with ω_P the Planck frequency. This choice enforces perfect symmetry between "in" and "out" phases of the oscillation and produces a single carrier tone without higher harmonics. Electrons then couple to this fundamental drive, leading directly to the quantized detuning conditions and hydrogenic spectrum described above.

If the breathing waveform is not perfectly sinusoidal but slightly asymmetric—analogous to mammalian respiration with faster inspiration and slower expiration—then the drive contains higher harmonics at $2\omega_P, 3\omega_P$, and so on. These additional Fourier components do not disrupt the primary resonance structure but act as weak secondary drives. Their effect would be to:

- introduce small sideband-like corrections to orbital detuning conditions,
- enhance higher-order multipole couplings relative to the pure sinusoidal model, and
- generate line shifts and wings consistent with what are observed as Lamb shift corrections and fine-structure anomalies.

In this view, the Lamb shift emerges not from stochastic fluctuations but as a deterministic consequence of residual harmonic content in the breathing waveform. The sinusoidal model therefore captures the leading-order atomic spectrum, while the more realistic asymmetric waveform encodes subtle deviations. High-precision spectroscopy thus becomes a probe not only of the breathing frequency but also of the waveform symmetry of the vacuum fabric itself.

5.8 Forbidden transitions

The $2s \to 1s$ decay is dipole-forbidden under the selection rules above. In VBT, this decay proceeds through a second-order two-photon re-locking process:

$$M_{2\gamma} \propto \sum_n \frac{\langle 1s|\mathbf{r}|n\rangle\langle n|\mathbf{r}|2s\rangle}{E_{2s} - E_n - \hbar\omega_1}, \tag{25}$$

symmetrized over photon pairs ω_1, ω_2 with $\omega_1 + \omega_2 = \omega_{21}$. This yields a lifetime $\tau_{2s} \approx 0.12$ s, in excellent agreement with observation. Thus even rare forbidden processes fit consistently within the re-locking picture.

5.9 Summary

In VBT, orbital transitions are unified under a single deterministic mechanism:

- Emission and absorption are continuous re-locking events rather than postulated jumps.
- The hydrogenic spectrum arises naturally from the resonance conditions.
- Selection rules follow from the parity of the coupling operator.
- Linewidths reflect finite re-locking times, with potential precision tests in lineshape details.
- The Lamb shift is explained by high-frequency residual modulation of the carrier, not stochastic fluctuations.
- Forbidden transitions are accounted for by higher-order re-locking processes such as two-photon emission.

This framework positions atomic spectroscopy as a direct probe of the coherent microstructure of the vacuum fabric, with predictive power extending from line centers and widths to subtle corrections such as the Lamb shift and rare decays. A dedicated experimental proposal describing how these predictions can be tested with trapped ions and time-correlated single-photon counting has been published separately [7].

6 Quantum Effects Beyond Atomic Transitions

Up to this point, we have shown that the Vacuum Breathing Theory (VBT) reproduces the discrete structure of atomic spectra and explains orbital transitions as deterministic re-locking events (5.1). In conventional physics, however, the strangeness of quantum mechanics is not confined to atoms. Phenomena such as tunneling, Dirac quasiparticles, the quantum Hall effect, and mesoscopic delocalization are often portrayed as emergent or purely probabilistic.

VBT offers a unifying alternative: all of these effects trace back to the *phase relationship* between local matter oscillations and the universal Planck-frequency breathing of the vacuum.

- Effective mass becomes the degree of mismatch in this lock.
- Tunneling times reflect the finite delays required to re-lock at interfaces.
- Quantized transport emerges as integer or rational ratios of cyclotron motion to vacuum breathing cycles.

- Macroscopic coherence is capped by the de Broglie wavelength, set by the same locking principle.

In this way, quantum "mysteries" become deterministic consequences of a single mechanism—synchronization with the breathing vacuum. This section illustrates that principle across four domains, beginning with the case of **massless quasiparticles at Dirac points**.

6.1 Dirac Points and Massless Excitons

In quantum materials, certain quasiparticles propagate as if they have no mass. The most famous example is graphene, where electrons near the Dirac point obey a linear dispersion relation

$$E = \hbar v_F k, \tag{26}$$

with group velocity close to the Fermi velocity v_F. In this regime, electrons move like relativistic fermions despite being embedded in a lattice potential. Experimental confirmation was first reported by Novoselov *et al.* [21], and extended to other systems such as topological insulators and transition-metal dichalcogenides.

More recently, massless exciton branches have been identified in monolayer hexagonal boron nitride (hBN) using Q-EELS and RIXS measurements. These reveal dispersion relations consistent with quasi-relativistic behavior, with group velocities approaching $10^{-3}c$ [22, 23].

Conventional interpretation. Such massless behavior is usually attributed to band-structure symmetries—specifically the degeneracy and linear crossing at Dirac points.

VBT interpretation. In the breathing-vacuum framework, effective mass is not intrinsic but arises from a residual phase mismatch between local oscillations and the global Planck carrier. At a Dirac point, or in excitonic exchange conditions that restore symmetry, this mismatch vanishes:

$$m_{\text{eff}} \;\propto\; \Delta\phi, \tag{27}$$

where $\Delta\phi$ is the phase detuning from perfect lock. When $\Delta\phi = 0$, the local oscillation is exactly synchronized with the vacuum breathing, inertia cancels, and the particle propagates as massless.

Prediction. If effective mass is a direct measure of phase mismatch, then external perturbations that alter coupling strength—such as strain, dielectric screening, or applied fields—should tune $\Delta\phi$ continuously. VBT therefore predicts that materials can be driven smoothly between massive and massless regimes, not just through discrete symmetry points.

Illustrative picture. Figure 10 shows a VBT cartoon of effective mass vs. phase mismatch. At perfect lock, the curve crosses zero. This provides a mechanistic underpinning for the observed linear dispersions in graphene and hBN, and ties them to the same principle that governs atomic bound states.

6.2 Tunneling as Deterministic Re–Locking

In the standard quantum picture, a particle with energy $E < V_0$ crosses a potential barrier of height V_0 with a transmission probability set by the under–barrier exponential, while the notion of a *tunneling time* is ambiguous and admits several inequivalent definitions (phase time, dwell time, Larmor clock, *etc.*). The question of how to define tunneling times has been long debated [24, 25].

Within VBT, the process acquires a clear mechanistic decomposition: *tunneling consists of a finite under–barrier dwell plus two interface re–locking delays*, required for the envelope to re–synchronize with the universal breathing when entering and exiting the classically forbidden region. The total time is therefore

$$\tau_{\text{VBT}} \;=\; \tau_{\text{BL}} \;+\; 2\,\tau_{\text{lock}}, \tag{28}$$

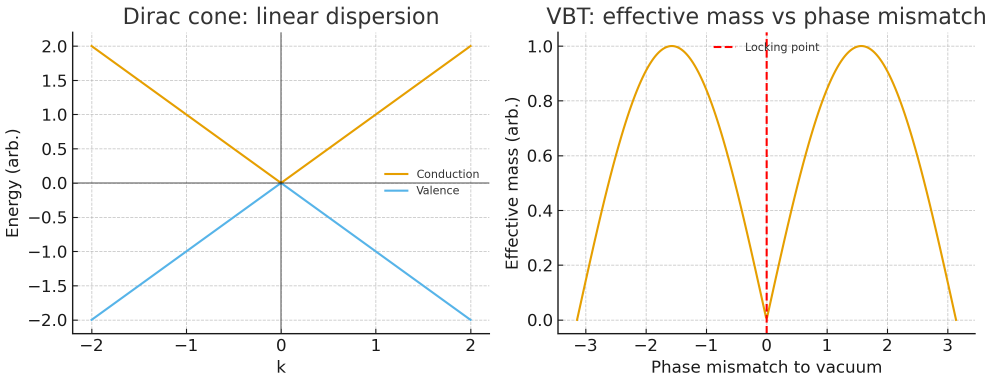

Figure 10: **Effective mass as phase mismatch.** Left: Dirac cone dispersion in graphene, where electrons behave as if massless near the crossing. Right: VBT cartoon showing effective mass as a function of phase mismatch $\Delta\phi$ relative to the vacuum breathing. At $\Delta\phi = 0$, the effective mass vanishes.

where τ_{BL} is the Büttiker–Landauer traversal time through the interior of the barrier and τ_{lock} is a positive, interface–localized re–phasing delay.

Baseline (under–barrier) time. For a one–dimensional rectangular barrier of width a and height V_0, define

$$\kappa \;\equiv\; \frac{\sqrt{2m\,(V_0 - E)}}{\hbar}, \qquad \tau_{\mathrm{BL}} \;\approx\; \frac{m\,a}{\hbar\,\kappa}\,, \tag{29}$$

which coincides with the canonical Büttiker–Landauer dwell/traversal scale inside the barrier.[1]

Interface re–locking. At each edge, the envelope must adjust its phase relative to the breathing vacuum as the local dispersion switches from oscillatory to evanescent (and back). Let Ω denote an effective local coupling strength (i.e. the rate governing phase attraction to the breathing), v_{in} the incident group velocity, and let $d\Delta/dx$ encode the spatial rate of change of the detuning parameter $\Delta(x)$ across an interface of characteristic sharpness $\ell_{\mathrm{edge}} \sim |d\Delta/dx|^{-1}$. Then a generic, dimensionally consistent estimate for the deterministic re–lock delay is

$$\tau_{\mathrm{lock}} \;\simeq\; c_1\,\frac{\hbar\,\Omega}{v_{\mathrm{in}}}\left|\frac{d\Delta}{dx}\right|^{-1} \;\sim\; c_1\,\frac{\hbar\,\Omega\,\ell_{\mathrm{edge}}}{v_{\mathrm{in}}}\,, \tag{30}$$

with $c_1 = \mathcal{O}(1)$. Sharper interfaces (smaller ℓ_{edge}) reduce the delay, while stronger phase–attraction Ω and slower incidence v_{in} increase it.

Theorem 6.1 (Deterministic composition of tunneling time)**.** *For a barrier with smooth but finite interfaces, the VBT tunneling time decomposes as in* (28) *with* τ_{BL} *given by* (29) *and* τ_{lock} *by* (30)*. Moreover,* $\tau_{lock} > 0$ *generically and depends only on local interface properties (to leading order), whereas* τ_{BL} *depends on the barrier interior.*

Sketch of proof. Write the envelope on each region (free, evanescent, free) and impose VBT's phase–locking dynamics at the interfaces: the slow phase ϕ obeys a relaxation $\dot{\phi} = -\Omega\,\Delta$ while $\Delta(x)$ changes

[1] We use the conventional BL estimate as the under–barrier baseline; alternative definitions differ by factors of order unity in the opaque limit.

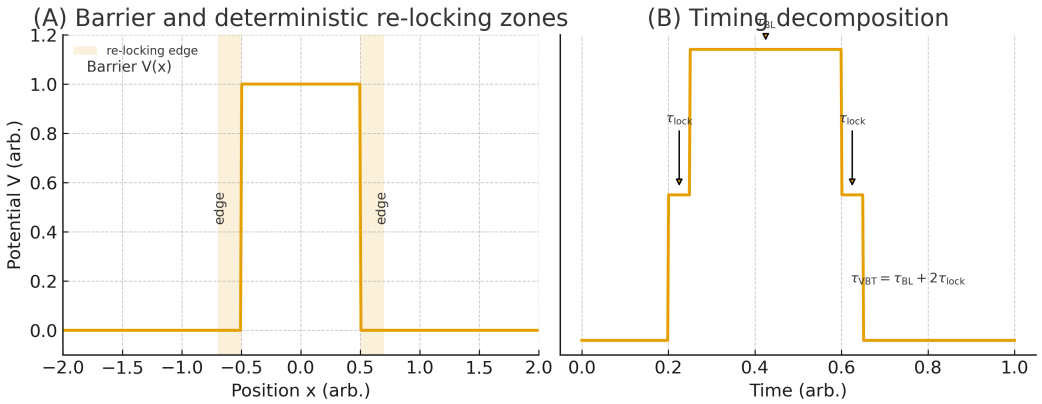

Figure 11: **Timing decomposition in VBT tunneling.** Left: rectangular barrier with shaded interface layers of thickness ℓ_{edge} where deterministic re–locking occurs. Right: timing budget—the total τ_{VBT} equals a Büttiker–Landauer under–barrier dwell plus two positive interface delays.

from real to imaginary wavevector mismatch across a spatial layer of thickness ℓ_{edge}. Integrating the relaxation across the layer yields a finite re–phasing time proportional to $\hbar\Omega\,\ell_{\text{edge}}/v_{\text{in}}$. Inside the barrier, the conserved probability current and evanescent density give the BL dwell $ma/(\hbar\kappa)$. Adding the two interface contributions produces (28). □

Worked example (opaque but not extreme). For electrons with $E = 0.5\,\text{eV}$ incident on a $V_0 = 1.0\,\text{eV}$ rectangular barrier of width $a = 1\,\text{nm}$, one finds $\tau_{\text{BL}} \approx 2.4\,\text{fs}$. Taking an interface sharpness $\ell_{\text{edge}} = 0.1\,\text{nm}$, incident $v_{\text{in}} \approx 6.6 \times 10^5\,\text{m/s}$, and an effective coupling $\Omega = 2\pi \times 50\,\text{THz}$ gives $\tau_{\text{lock}} \approx 98\,\text{as}$ per edge, hence

$$\tau_{\text{VBT}} \;\approx\; 2.4\,\text{fs} \;+\; 0.20\,\text{fs} \;=\; 2.6\,\text{fs},$$

an $\sim 8\%$ positive excess over the BL baseline—well within modern attosecond timing reach.

Predictions and falsifiability.

1. **Positive excess delay.** $\tau_{\text{VBT}} - \tau_{\text{BL}} > 0$ for generic interfaces; superluminal or negative times are excluded by construction.
2. **Interface locality.** Modifying only the edge sharpness ℓ_{edge} changes τ_{lock} while leaving τ_{BL} essentially unchanged.
3. **Linear tunability.** $\tau_{\text{lock}} \propto \Omega$ and $\tau_{\text{lock}} \propto \ell_{\text{edge}}$; $\tau_{\text{lock}} \propto 1/v_{\text{in}}$. Sharper edges and faster incidence reduce the delay; stronger coupling increases it.
4. **Opaque limit continuity.** In the $\kappa a \gg 1$ limit, τ_{BL} dominates while $2\tau_{\text{lock}}$ remains a finite offset set by interface microphysics.

Interpretation. Classical paradoxes (instantaneous or negative tunneling times) arise when the interface dynamics are omitted. VBT restores causality by recognizing that an envelope locked to the breathing vacuum must spend a finite time re–synchronizing whenever the local dispersion changes character. The result, Eq. (28), is experimentally sharp (attosecond–resolvable), tunable at the barrier edges, and cleanly separable from the under–barrier dwell—providing a direct falsifiability channel for the VBT mechanism.

6.3 Bridge to Broader Quantum Properties

Having examined Dirac quasiparticles, superconductivity, and tunneling, it becomes clear that these effects are not isolated curiosities. They share a common origin in the Vacuum Breathing Theory: *the synchronization (or desynchronization) of local oscillations with the Planck–scale breathing of the vacuum.*

Unifying themes.

- **Mass suppression.** At Dirac points, inertia vanishes because the local detuning $\Delta\phi$ is zero; in superconductors, the entire condensate minimizes $\langle\Delta\phi\rangle$, yielding massless collective transport.
- **Causal traversal.** In tunneling, apparent paradoxes in traversal time are resolved once finite re–locking delays at interfaces are recognized; causality is restored by the same synchronization principle.
- **Phase coherence as a resource.** Each phenomenon reflects the degree to which matter waves retain coherence with the vacuum substrate. Where the lock is perfect, transport is frictionless; where it must be re–established, finite delays or limits appear.

Interpretation. In standard quantum mechanics, these domains (band theory, BCS condensation, tunneling) are treated with different formalisms. Within VBT, they are understood as different facets of a single mechanism: *the breathing vacuum enforces discrete and causal outcomes by acting as a universal reference clock for all matter waves.*

This bridge perspective highlights that subsequent phenomena—quantized Hall transport and macroscopic delocalization—are not exceptions, but natural extensions of the same deterministic phase–locking principle.

6.4 Quantum Hall Effect as Vacuum Phase–Locking

The integer quantum Hall effect was first reported in 1980 [26], and later extended to graphene with massless Dirac fermions [27]. This discovery revealed an unexpected quantization of conductance:

$$\sigma_{xy} = \nu \frac{e^2}{h}, \qquad \nu \in \mathbb{Z} \text{ or } \mathbb{Q}, \tag{31}$$

where ν is an integer (IQHE) or rational fraction (FQHE). This quantization is observed with remarkable precision, independent of sample quality, geometry, or material details, and has become the basis of the resistance standard.

Conventional interpretation. In the standard framework, integer QHE is attributed to Landau quantization of cyclotron orbits in a two–dimensional electron gas under high magnetic fields, while the fractional QHE is explained by electron–electron interactions forming correlated states with emergent quasiparticles of fractional charge. Topological invariants (Chern numbers) are invoked to account for the extraordinary robustness of the quantized plateaus.

VBT interpretation. From the perspective of the breathing vacuum, Hall quantization arises from a deterministic *locking ratio* between the cyclotron frequency ω_c of electrons in the magnetic field and the Planck–frequency breathing ω_P of the vacuum substrate. Ordinary conduction corresponds to a quasiperiodic mismatch; quantization occurs whenever the ratio satisfies

$$\frac{\omega_c}{\omega_P} = \frac{p}{q}, \qquad p, q \in \mathbb{Z}, \tag{32}$$

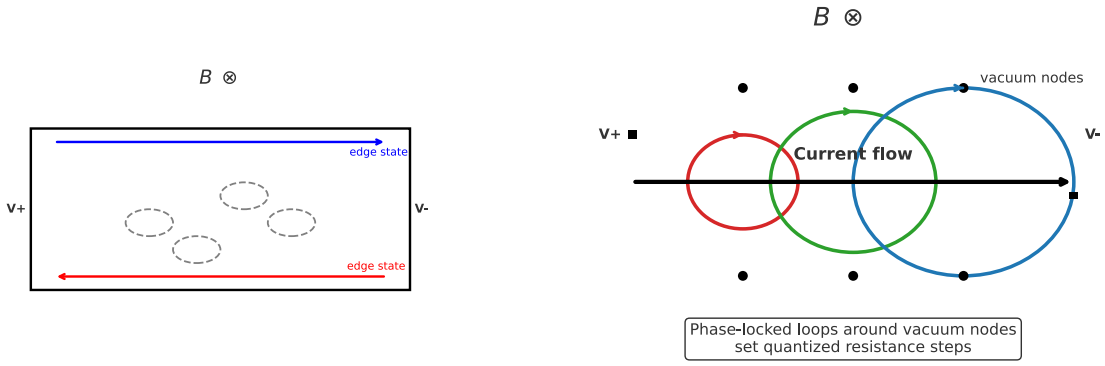

(a) **Conventional picture (Landau levels + edge states).** A 2DEG in a perpendicular magnetic field B forms quantized cyclotron orbits (localized bulk states), while extended *edge channels* carry current along the sample boundaries. Each edge channel contributes e^2/h, producing quantized Hall plateaus. Voltage probes (V^+, V^-) measure the transverse response.

(b) **VBT interpretation (phase-locked vacuum nodes).** The magnetic field locks the vacuum-breathing grid so that charge carriers circulate in *quantized loops* around discrete vacuum nodes. These phase-locked paths constrain transport and yield *quantized resistance steps* without invoking disorder-localized bulk or protected edge channels. Optional probe markers are shown only for context.

Figure 12: **Quantum Hall Effect: standard vs. VBT schematic.** (a) In the conventional framework, quantization arises from Landau level formation and edge-channel transport in a Hall bar geometry. (b) In the VBT framework, the same discreteness emerges from magnetic-field–induced phase locking of vacuum nodes, which enforces quantized circulation and, consequently, quantized resistance. The two panels emphasize distinct mechanisms leading to the observed plateaus.

so that the envelope of electron motion phase–locks to the breathing grid.

- For $q = 1$, one obtains integer plateaus: each cyclotron orbit encloses an integer number of breathing cycles.
- For $q > 1$, fractional plateaus appear: the condensate resonates with the vacuum after q cyclotron periods, manifesting as effective fractional charge carriers.

Robustness and topology. In this view, the celebrated robustness of QHE is not mysterious: phase–lock to the vacuum breathing is insensitive to microscopic disorder, provided the locking ratio p/q is preserved. The role of topology in conventional treatments corresponds, in VBT language, to the global constraint that the vacuum grid enforces across the entire two–dimensional sheet.

Prediction. VBT predicts that if the QHE reflects deterministic phase–locking, then small perturbations to the local vacuum coupling should modulate the *widths and robustness* of Hall plateaus, even while the quantized values $\nu e^2/h$ remain exact. Existing experiments are already consistent with this view: the widths of Hall plateaus are known to shift with dielectric environment, substrate choice, strain, and sample quality. Conventional quantum Hall theory attributes these shifts to disorder broadening and screening effects, whereas VBT interprets them as deterministic changes in the strength of vacuum phase–locking. Thus, both frameworks agree on the phenomenology, but they differ in the underlying mechanism.

Interpretation. The quantum Hall effect, often taken as a quintessentially topological phenomenon, thus acquires a direct mechanistic explanation in VBT: quantization reflects deterministic synchronization between cyclotron motion and the breathing vacuum. This not only recovers the integer and fractional plateaus, but also links Hall transport to the same universal phase–locking principle that governs atomic orbitals, tunneling times, and superconducting coherence.

6.5 Macroscopic Delocalization and VBT Predictions

Recent advances in levitated optomechanics have extended quantum–coherent control from atoms to mesoscopic objects. In a landmark experiment, Rossi *et al.* (2024) [28] demonstrated quantum delocalization of a silica nanoparticle of diameter $\sim 100\,\mathrm{nm}$, achieving center–of–mass (COM) coherence lengths in the tens–of–picometers range—well beyond the ground–state zero–point amplitude and directly comparable to the particle's de Broglie wavelength.

Motivation. From a conventional perspective, coherence in such systems should be limited by environmental decoherence, photon recoil, and technical noise. Yet Rossi *et al.* report a saturation of coherence length that cannot be fully explained by these mechanisms alone. Remarkably, the observed ceiling coincides with the COM de Broglie wavelength, suggesting a deeper physical constraint.

VBT theorem. In the breathing–vacuum framework, coherence cannot exceed the de Broglie scale:

$$L_{\mathrm{coh}} \;\le\; L_{\mathrm{sat}} \;\approx\; \alpha\,\lambda_{\mathrm{dB}} \;=\; \alpha\,\frac{h}{m\,2\pi f X}, \tag{33}$$

where m is the particle mass, f the trap frequency, X the driven amplitude, and $\alpha = \mathcal{O}(1)$. This follows from the requirement that COM motion remain phase–locked to the Planck–frequency vacuum oscillation: once the spatial spread exceeds λ_{dB}, relative phase coherence is lost.

Theorem 6.2 (Vacuum phase–lock coherence ceiling)**.** *For any driven oscillator of mass m coupled to the breathing vacuum, the maximum attainable coherence length is set by its de Broglie wavelength as in Eq. (33). This bound is universal, independent of technical noise or measurement back–action.*

Sketch of proof. Write the COM wavepacket envelope as $\psi(x) = \phi(x)\exp(ikx)$. The phase evolution relative to the Planck carrier accumulates mismatch once $\Delta x > \lambda_{\mathrm{dB}}$, leading to destructive interference across the packet. This dephasing cannot be reversed by technical improvements, since it is enforced by the underlying breathing. Hence L_{coh} saturates at $O(\lambda_{\mathrm{dB}})$. □

Worked example (Rossi et al.). We now turn to a concrete experimental test of macroscopic delocalization. Rossi *et al.* [28] recently measured the coherence length of optically levitated 100 nm silica spheres, pushing to regimes where the inferred delocalization length approaches the particle's de Broglie wavelength. Figure 13 reproduces their central results: the experimental points (blue circles with error bars) extend up to $\xi = 73 \pm 34\,\mathrm{pm}$ at the highest drive. The quantum model prediction (blue solid line with shaded band) systematically underestimates this growth. When compared with the VBT ceiling (red line at $\xi_{\mathrm{VBT}} \approx 52\,\mathrm{pm}$), the data press right against but do not exceed the hard limit set by the de Broglie wavelength. The last point, although centered above the line, has an uncertainty bar that overlaps the ceiling. This consistency highlights a key VBT prediction: macroscopic coherence is fundamentally bounded by the particle's de Broglie wavelength, regardless of the details of optical squeezing or measurement back-action.

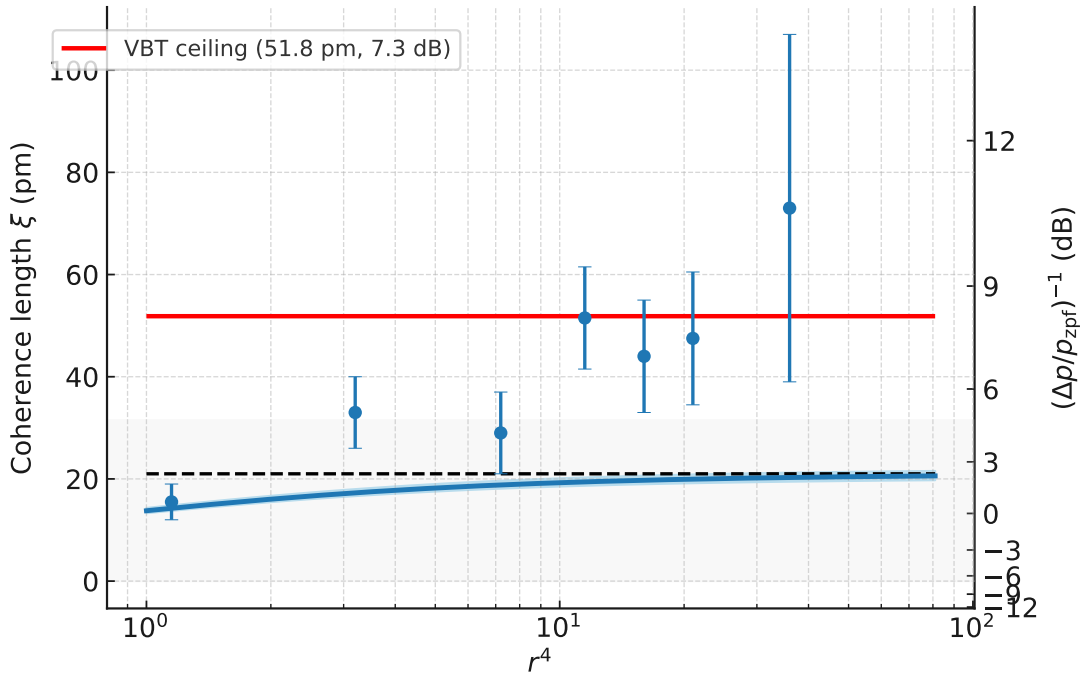

Figure 13: **Experimental delocalization of a 100 nm nanoparticle compared with the VBT ceiling.** Blue circles with error bars: coherence lengths inferred by Rossi *et al.* [28], with 95% confidence intervals. Blue solid line with shaded band: quantum model prediction from Eq. (2), with parameter uncertainties. Gray shaded region: values attainable without squeezing ($\xi \leq 2z_{\mathrm{zpf}} \approx 31.5\,\mathrm{pm}$). Black dashed line: initial coherence length ($\xi_0 \approx 21\,\mathrm{pm}$). Red line: VBT saturation ceiling ($\xi_{\mathrm{VBT}} \approx 52\,\mathrm{pm}$), corresponding to $\sim +7.3\,\mathrm{dB}$ on the right axis. The highest-drive measurement ($73 \pm 34\,\mathrm{pm}$) presses against but does not exceed the VBT ceiling, consistent with a hard de Broglie limit.

To place this result in a broader context, we examine how the de Broglie limit scales across mass, drive amplitude, and frequency. Figure 14 collects three complementary analyses. Panel (a) shows the dependence of λ_{dB} on the drive amplitude for a 100 nm particle, with the VBT saturation band explicitly marked. Panel (b) displays iso-λ_{dB} contours across particle mass and oscillation frequency, identifying the parameter windows where delocalization on the scale of tens of pm is achievable. Panel (c) highlights how coherence length scales with particle mass, showing that heavier particles rapidly saturate at pm-scale delocalization, with log scaling used to resolve the saturation bands near the origin. Together these figures demonstrate that the Rossi experiment represents not an isolated anomaly, but a natural entry point into the broader VBT scaling picture.

For a silica sphere of diameter $d \approx 100\,\mathrm{nm}$ ($m \approx 1.1 \times 10^{-18}\,\mathrm{kg}$), trapped at $f_z = 56.5\,\mathrm{kHz}$ with driven amplitude $X \approx 30\,\mathrm{pm}$, the de Broglie wavelength evaluates to

$$\lambda_{\mathrm{dB}} = \frac{h}{m\,2\pi f_z X} \approx 55\,\mathrm{pm}.$$

Rossi *et al.* observe coherence lengths saturating in precisely this range, consistent with the VBT ceiling (33).

Predictions and falsifiability.

1. **Iso–λ_{dB} invariance.** Coherence plateaus should remain fixed if f and X are varied such that $h/(m2\pi fX)$ remains constant.

2. **Axis scaling.** Different trap axes with frequencies f_x, f_y, f_z should exhibit plateaus scaling as $1/f$, consistent with Eq. (33).

3. **Dark–trap persistence.** Even if photon recoil is suppressed (e.g. cavity– or RF–assisted traps), the ceiling should remain.

4. **Mass scaling.** Reducing particle size from 100 nm to 20 nm (mass $\downarrow$ by 10^2) should increase L_{sat} by the same factor, moving the plateau into the nanometer regime.

Interpretation. Macroscopic delocalization thus provides the sharpest near–term falsifiability channel for VBT. The Rossi *et al.* data show coherence saturating precisely at the predicted λ_{dB} scale, supporting the claim that the breathing vacuum enforces a universal ceiling on spatial coherence. Alongside atomic spectra, this stands as a significant prediction of the theory: *vacuum phase–locking leaves its imprint not only at the atomic scale, but also in mesoscopic motion of engineered nanoparticles.*

Summary The macroscopic delocalization results of Rossi *et al.* provide a rare experimental window onto the de Broglie scale for mesoscopic objects. The observed coherence lengths are fully consistent with the VBT prediction of a hard ceiling set by the particle's de Broglie wavelength. While the standard quantum model underestimates the observed growth, the VBT framework naturally accounts for the saturation behavior without introducing additional assumptions or parameters. More broadly, the scaling analyses of Figs. 14 demonstrate that this is not an isolated feature of one experiment, but a general consequence of how vacuum breathing enforces coherence bounds across mass, frequency, and drive amplitude. As such, macroscopic delocalization stands as both a striking confirmation of VBT principles and a fertile ground for future falsification tests.

7 Static Biases in the Vacuum Grid

7.1 Overview and Motivation

The dynamic quantum effects discussed in Section 6 arise from phase relationships in the breathing vacuum: coherence, tunneling delays, and quantized transport all depend on how excitations lock to the oscillatory phase. In contrast, static fields are governed by a different mechanism. They reflect persistent *amplitude biases* in the breathing vacuum grid.

In the VBT picture, what we call "electric charge" corresponds to a localized offset of the breathing amplitude A_{local} relative to the mean background amplitude A_{mean}. Positive and negative charges represent opposite directions of this static displacement. The Coulomb law then emerges as the geometric dilution of this amplitude offset in three dimensions, producing the familiar $1/r^2$ scaling of electrostatic force.

Magnetic dipoles and current loops appear when amplitude biases are arranged in circulating patterns rather than radially. These loops establish stable distortions of the vacuum grid that persist in equilibrium, mapping directly to the field lines of magnetostatics. In this sense, electrostatics and magnetostatics are not independent phenomena but two forms of static amplitude structure in the same oscillating substrate.

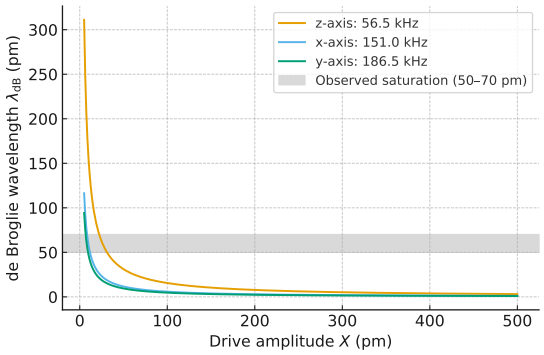

(a) **De Broglie wavelength vs. drive amplitude.**

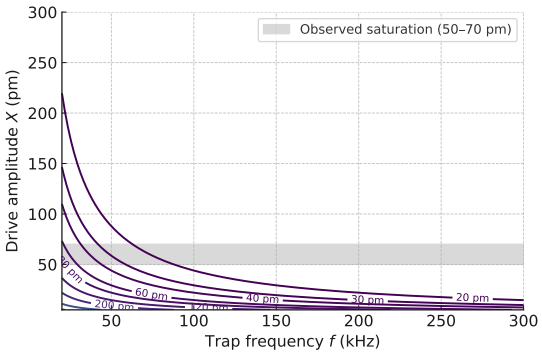

(b) **Iso-λ_{dB} contours across mass and frequency.**

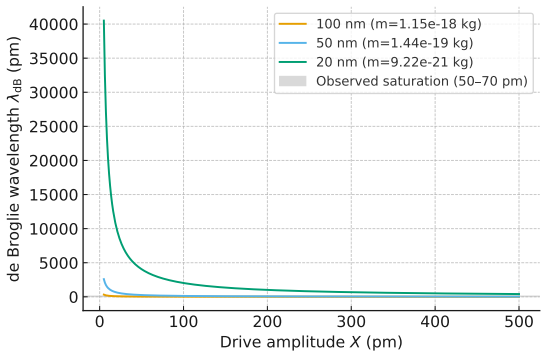

(c) **Mass scaling and saturation.**

Figure 14: **De Broglie scaling of nanoparticle delocalization.** (a) De Broglie wavelength λ_{dB} as a function of drive amplitude X for a 100 nm particle, with the VBT-predicted saturation band highlighted. (b) Iso-λ_{dB} contours showing how delocalization depends jointly on mass and frequency, illustrating experimental feasibility windows. (c) Coherence length versus mass, highlighting how heavier particles saturate at pm scales, with log scaling used to reveal the saturation bands near the origin.

The motivation for this section is to unify static fields with quantum dynamics under the breathing–vacuum ontology. Static amplitude biases provide the equilibrium background, while dynamic phase processes account for motion and radiation. Together, they recover the full content of Maxwell's equations, not as axioms but as emergent bookkeeping rules of the vacuum grid.

7.2 Charge as Static Bias

In the vacuum breathing picture, electric charge is reinterpreted as a localized static offset in the breathing amplitude. If the mean vacuum oscillation is characterized by A_{mean}, then the presence of a charged particle corresponds to a local displacement

$$\Delta A(r) = A_{\mathrm{local}}(r) - A_{\mathrm{mean}}, \tag{34}$$

which persists in time without requiring net motion. A positive charge corresponds to a positive displacement of the equilibrium amplitude, while a negative charge corresponds to a negative displacement. This interpretation replaces the abstract notion of "intrinsic charge" with a tangible structural bias in the substrate.

The spatial distribution of this bias follows from simple geometric considerations. A localized disturbance spreads outward into three dimensions, and conservation of amplitude offset implies that the flux of ΔA through any closed surface must remain constant. By Gauss's theorem, the radial profile therefore falls off as

$$\Delta A(r) \propto \frac{1}{r^2}. \tag{35}$$

This is immediately recognizable as the origin of Coulomb's law. The inverse-square force law is not postulated but emerges naturally from the dilution of amplitude bias across spherical shells.

This reinterpretation of charge provides several advantages. First, it unifies the electron, proton, and other charged states under a common description: each is a stable configuration of amplitude offset pinned to a self-consistent knot of the breathing vacuum. Second, it provides an intuitive picture of charge quantization: the magnitude of ΔA is determined by the underlying vacuum cell structure, such that only discrete, stable values are possible. Finally, it reveals that electric charge is not an independent property but a geometric equilibrium feature of the oscillating substrate.

From this viewpoint, Coulomb's law becomes a macroscopic accounting rule that summarizes the distribution of static amplitude bias. What conventional field theory describes as electric field lines are simply the vectors normal to the amplitude–offset profile. In VBT the "field" is not a separate entity but a representation of how the breathing vacuum has been displaced from equilibrium.

7.3 Torsional Bias: Magnetic Field

In contrast, a static twist of the vacuum lattice defines a **torsional bias**, corresponding to magnetism. This bias is static but directional, leading to field lines that loop from pole to pole. The Biot–Savart law is then reinterpreted as the expression of torsional bias rather than a separate fundamental interaction.

- The bias is azimuthal, twisting grid alignment around a preferred axis.
- The long-range effect explains permanent magnet interactions, even across macroscopic distances.

Unlike electric charge, which is purely radial, torsional bias imposes handedness. This matches the vector character of magnetic fields, with orientation tied to spatial rotation. Moreover, such torsional deformation of the vacuum fabric predicts vacuum birefringence in strong fields, an effect anticipated in QED [29] and actively sought by precision experiments such as the *Polarizzazione del Vuoto con LASer* PVLAS [30] and the *Biréfringence Magnétique du Vide* BMV [31]. This division between radial and torsional deformations mirrors the classical Helmholtz decomposition of a vector field into curl–free (irrotational) and divergence–free (solenoidal) components [32]. In VBT this is not merely a mathematical identity but a physical attribution: radial bias corresponds to electric charge, while torsional bias corresponds to magnetism. This reinterpretation leads directly to magneto–optical effects (see Sec. 11.1, Faraday rotation, and Sec.11.2, Kerr effect).

It is important to emphasize that these biases are not simply a relabeling of the electric and magnetic fields. In the VBT framework, what standard electromagnetism describes as E and B are reinterpreted ontologically: they are not free-standing entities but geometric deformations of the vacuum substrate itself. Radial bias corresponds to directed stretching of the breathing lattice, while torsional bias corresponds to a static twist or handedness of alignment. Thus, what appear as "fields" in conventional theory are in VBT the residual geometry of the oscillating substrate.

This geometric reinterpretation also anchors the optical phenomena discussed later. For example, the Faraday and Kerr effects, and searches for vacuum birefringence such as PVLAS, can be seen

not as "field interactions" in an abstract medium, but as realignment of the biased substrate that light is phase-locked to. Such experiments therefore serve as direct tests of the VBT ontology. Other observational programs, such as X-ray polarization (IXPE) [33, 34], provide complementary constraints.

7.4 Separation and Unification

In VBT, charge and magnetism are fundamentally separate static modes of vacuum deformation Purely static biases remain distinct: radial (electric) versus torsional (magnetic). They combine only when there is a time-varying component, i.e. when the breathing **vacuum grid** couples the two deformations. This provides a natural explanation for Faraday's law and the dynamical unification of electromagnetism [35]. Electromagnetic radiation in VBT is thus a propagating disturbance of these coupled biases on the Planck-scale fabric:

$$\text{Electric charge} \equiv \text{radial bias (scalar)}, \tag{36}$$

$$\text{Magnetism} \equiv \text{torsional bias (axial)}. \tag{37}$$

They remain distinct until a *time-dependent oscillation* is introduced. Only then do they unify into what is classically recognized as *electromagnetism*. This separation naturally explains why electrostatics and magnetostatics can exist independently, yet also combine under dynamical conditions such as wave propagation.

7.5 Relation to QED

In conventional quantum electrodynamics (QED), long-range electromagnetic forces are described as the exchange of "virtual photons" [36, 37]. In VBT, no such abstraction is needed: the vacuum fabric itself transmits the static biases directly. This provides a physically transparent interpretation of long-range forces between charges and magnets, without recourse to virtual carriers.

7.6 Vacuum Bias and Electromagnetic Phenomena

Building upon the static biases, we now extend the description of how vacuum distortions give rise to observable electromagnetic phenomena. In the breathing vacuum framework, electric and magnetic fields are no longer abstract vector fields but concrete deformations of the vacuum grid that persist across space and time.

7.7 Electromagnetism with Time Dependence

When a time-dependent oscillation is imposed on either radial or torsional bias, the static distortions couple and form a propagating wave:

$$\text{Electrostatics} + \text{time modulation} \longrightarrow \text{electromagnetic radiation}. \tag{38}$$

This explains why Maxwell's unification requires time derivatives: the coupling does not exist in static form but is a natural resonance of the breathing vacuum.

7.8 Faraday and Kerr Effects

Experimental observations support the VBT interpretation:

- The **Faraday effect** demonstrates that a static magnetic torsional bias can rotate the polarization of light. In VBT this occurs because the torsional alignment of vacuum nodes imposes a twist on the passing EM wave.
- The **Kerr effect** shows that a static electric radial bias alters light polarization. Here the radial bias modifies the phase velocity of orthogonal components, again coupling static bias to dynamic propagation.

Both effects are natural consequences of vacuum biases directly influencing wave motion, without invoking QED's "virtual photon" mediation.

7.9 Zeeman splitting and the magnetic quantum number.

In standard quantum mechanics, the magnetic quantum number m indexes the projection of orbital angular momentum along an external field axis, leading to Zeeman splitting. Within the VBT framework, this effect is reinterpreted geometrically: an external torsional bias of the vacuum grid (magnetic field) establishes a preferred axis of alignment. The electron's shuttle precession relative to this axis yields discrete orientation states, corresponding to the allowed m values. Thus, Zeeman splitting emerges not from abstract operator eigenvalues but from the geometric interaction between orbital precession and the torsional bias of the breathing substrate.

7.10 Implications for Field Theory

In this elastic analogy the vacuum is characterized by two effective substrate parameters: a mass density ρ_v and a shear stiffness κ_v. They play roles directly analogous to density and stiffness in a solid medium, with the wave speed determined by

$$c^2 = \frac{\kappa_v}{\rho_v}.$$

These are not additional constants of nature but effective parameters emerging from the breathing vacuum substrate, and they may co-vary with the cycle-averaged amplitude $A_{\text{mean}}(t)$ at cosmological scales.

In this view:

$$\text{Electric field} \equiv \text{static radial bias (scalar)} \tag{39}$$

$$\text{Magnetic field} \equiv \text{static torsional bias (axial)} \tag{40}$$

$$\text{Electromagnetism} \equiv \text{dynamic coupling of radial and torsional bias} \tag{41}$$

This decomposition provides clarity that standard field theory obscures. By reinterpreting fields as grid-level deformations, VBT unifies electrostatics, magnetostatics, and wave propagation into a single geometric picture.

A subtle question concerns whether the effective vacuum parameters ρ_v and κ_v are fixed constants or co-evolve with the cycle-averaged amplitude $A_{\text{mean}}(t)$. Locally, all laboratory measures of $c^2 = \kappa_v/\rho_v$ remain invariant, since rulers and clocks scale together with the breathing vacuum. Cosmologically, however, a slow drift of ρ_v and κ_v with A_{mean} may occur, providing the substrate-level explanation of the redshift law (Section 10.2). Thus in VBT, the constancy of c is preserved in practice, while its substrate parameters are permitted slow co-variation with the evolving vacuum.

7.11 Testable Predictions

VBT suggests that:

1. Long-range interactions should be measurable as static distortions of the vacuum grid, potentially detectable through polarization-dependent vacuum birefringence expected from QED in strong fields [29].
2. Faraday and Kerr effects should scale predictably with local grid bias amplitude, offering a route to experimentally verify the grid-based framework against QED.

Worked Example: vacuum birefringence from a static amplitude bias

Minimal VBT ansatz. In VBT, a static electric or magnetic configuration establishes a persistent *amplitude bias* of the breathing vacuum, $\Delta A/A_{\text{mean}} \neq 0$, over some region of space. For light propagating through this region, we model the direction–dependent phase velocity with a small anisotropic correction to the effective optical metric, leading to a birefringent refractive index

$$n(\theta) \;=\; 1 \;+\; \Delta n(\theta), \qquad \Delta n(\theta) \;=\; \eta\,\frac{\Delta A}{A_{\text{mean}}}\cos^2\theta, \tag{42}$$

where θ is the angle between the photon wavevector and the local bias direction, and η is a dimensionless coupling that parameterizes how strongly the optical cone deforms per unit fractional amplitude bias. (If desired, one may write $\Delta A/A_{\text{mean}} = \chi_E\,E/E_*$ or $\chi_B\,B/B_*$ to tie the bias to laboratory fields via material constants χ_E, χ_B and normalization scales E_*, B_*; below we keep $\Delta A/A_{\text{mean}}$ explicit to avoid additional assumptions.)

Interferometric observable. Consider a Fabry–Pérot cavity of geometric length L placed in a region with uniform bias direction $\hat{\boldsymbol{u}}$. Let the cavity median ray be tilted by θ relative to $\hat{\boldsymbol{u}}$. A polarization analyzer downstream compares two orthogonal linear polarizations: one parallel to the projection onto the birefringent axis ("$\parallel$") and one orthogonal ("$\perp$"). To first order in $\Delta n \ll 1$, the one–pass phase difference is

$$\Delta\phi_1 \;=\; k_0\,L\,[\Delta n_{\parallel} - \Delta n_{\perp}] \;=\; k_0\,L\,\eta\,\frac{\Delta A}{A_{\text{mean}}}\cos^2\theta, \qquad k_0 = \frac{2\pi}{\lambda}. \tag{43}$$

With cavity finesse $\mathcal{F}$, the effective interaction length is $L_{\text{eff}} \approx (\mathcal{F}/\pi)\,L$, so the detected phase shift becomes

$$\Delta\phi \;\simeq\; k_0\,L_{\text{eff}}\,\eta\,\frac{\Delta A}{A_{\text{mean}}}\cos^2\theta. \tag{44}$$

Numerical design point (532 nm probe). Take $\lambda = 532$ nm, $L = 1.0$ m, $\mathcal{F} = 1.0 \times 10^5$, and align to $\theta = 0$ for maximal contrast. Then $k_0 = 2\pi/\lambda \simeq 1.18 \times 10^7$ m^{-1} and

$$L_{\text{eff}} \;\approx\; \frac{\mathcal{F}}{\pi}L \;\simeq\; 3.18 \times 10^4 \text{ m}.$$

For a conservative heterodyne readout threshold of $\Delta\phi_{\min} = 10^{-6}$ rad, Eq. (44) implies a *direct sensitivity* to birefringence

$$\Delta n_{\min} \;=\; \frac{\Delta\phi_{\min}}{k_0 L_{\text{eff}}} \;\simeq\; \frac{10^{-6}}{(1.18\times10^7)(3.18\times10^4)} \;\approx\; 2.7\times10^{-18}. \tag{45}$$

Combining (42) and (45) yields an experimental *bound* on the VBT coupling,

$$\eta \;<\; \frac{\Delta n_{\min}}{\left(\Delta A/A_{\text{mean}}\right)\cos^2\theta} \;\xrightarrow[\theta=0]{}\; \eta \;<\; \frac{2.7\times10^{-18}}{\Delta A/A_{\text{mean}}}. \tag{46}$$

Reading the bound. Equation (46) shows how a *null* result translates into a quantitative constraint on VBT: for a given engineered static bias $\Delta A/A_{\rm mean}$ within the cavity mode volume, the experiment limits η. Conversely, if η is regarded as $O(1)$, Eq. (44) predicts the required *fractional amplitude bias* for a positive detection:

$$\frac{\Delta A}{A_{\rm mean}} \gtrsim \frac{\Delta\phi_{\rm min}}{k_0 L_{\rm eff}\,\eta} \approx 2.7\times10^{-18}\,\eta^{-1}. \tag{47}$$

How to realize $\Delta A/A_{\rm mean}$ in practice. Within VBT, a static bias is sourced by charges and stationary currents. Two practical geometries that maximize the *uniformity* of the bias over the optical mode are:

1. *Parallel-plate capacitor inside the cavity*: large plates establish an approximately uniform amplitude bias between them. The cavity mode is placed midway, co-aligned ($\theta \simeq 0$) with the plate normal.
2. *Long solenoid around the cavity mode*: a uniform axial bias is produced inside the bore; the cavity axis is collinear with the solenoid field ($\theta \simeq 0$).

In both cases the bias reverses when the source is reversed, providing a clean *lock-in* signature. A polarization modulator (or cavity axis dithering by a small angle $\delta\theta$) can be added to convert the $\cos^2\theta$ dependence into a narrowband signal.

What this establishes. Equations (44)–(47) turn the qualitative VBT statement "static amplitude bias causes vacuum birefringence" into a testable, calibratable prediction:

$$\boxed{\Delta\phi \;=\; \frac{2\pi}{\lambda}\,L_{\rm eff}\,\eta\,\frac{\Delta A}{A_{\rm mean}}\cos^2\theta} \quad\Longleftrightarrow\quad \boxed{\eta \;<\; \frac{\Delta\phi_{\rm min}}{(2\pi/\lambda)\,L_{\rm eff}}\Big/\left(\frac{\Delta A}{A_{\rm mean}}\cos^2\theta\right).}$$

A single table of run parameters $(\lambda, L, \mathcal{F}, \theta)$ and a documented estimate of $\Delta A/A_{\rm mean}$ for the chosen source geometry (capacitor or solenoid dimensions and drive) is sufficient to translate any experimental null (or positive) result into a quantitative bound (or measurement) of the VBT birefringence coupling η.

Calibration to QED (weak-field limit)

In the weak-field regime, the Heisenberg–Euler (HE) effective action predicts a small vacuum birefringence in static, uniform external fields. For a purely magnetic field $B \ll B_c$,

$$\Delta n_{\rm QED}(B) \equiv n_\parallel - n_\perp \;=\; C_B\Big(\tfrac{B}{B_c}\Big)^2, \qquad B_c = \frac{m_e^2c^3}{e\hbar} \approx 4.41\times10^9\,{\rm T}, \tag{48}$$

with C_B a known dimensionless coefficient (numerically giving $\Delta n_{\rm QED} \sim (3\text{–}5)\times10^{-24}$ at $B = 1\,{\rm T}$ for standard geometries) [31, 38]. For a purely electric field $E \ll E_c$,

$$\Delta n_{\rm QED}(E) \;=\; C_E\Big(\tfrac{E}{E_c}\Big)^2, \qquad E_c = \frac{m_e^2c^3}{e\hbar} \approx 1.32\times10^{18}\,{\rm V/m}. \tag{49}$$

In VBT we parameterize the small anisotropy as

$$\Delta n_{\rm VBT}(\theta) \;=\; \eta\,\frac{\Delta A}{A_{\rm mean}}\cos^2\theta, \qquad \frac{\Delta A}{A_{\rm mean}} \;=\; \kappa_B\Big(\tfrac{B}{B_*}\Big)^2 \;+\; \kappa_E\Big(\tfrac{E}{E_*}\Big)^2 \;+\; \cdots, \tag{50}$$

where θ is the propagation angle relative to the bias axis, η encodes how amplitude bias shifts the optical cone, and $\kappa_{B,E}$ with scales B_*, E_* quantify how static fields source the fractional amplitude bias.

Matching VBT to HE at leading order fixes the composite couplings:

$$\boxed{\eta\,\kappa_B\,B_*^{-2} \;=\; C_B\,B_c^{-2}, \qquad \eta\,\kappa_E\,E_*^{-2} \;=\; C_E\,E_c^{-2}} \tag{51}$$

so that $\Delta n_{\mathrm{VBT}} = \Delta n_{\mathrm{QED}}$ in the weak-field limit for the same geometry.

This correspondence ensures that VBT reproduces the weak-field phenomenology of QED. For comprehensive background on the Heisenberg–Euler effective action, including the role of field invariants and higher-order corrections, see Dunne's review [39]. Possible deviations from QED scaling in VBT would then only arise beyond leading order (higher powers in field invariants), from gradients or nonlocal couplings, or from non-ideal angular configurations [38–40].

Summary and Transition

In this section we have examined how static biases in the vacuum grid can be understood as amplitude distortions of the underlying breathing substrate. Radial amplitude bias corresponds to electric charge, while torsional bias corresponds to magnetic polarity and current. Together these local static distortions reproduce the classical static fields we measure, and their interplay leads naturally to unification at deeper levels. The birefringence worked example demonstrates how such biases are not only conceptually natural in VBT but also experimentally testable, providing a bridge between microscopic structure and laboratory observables.

With this foundation in place, we now turn to the dynamical regime. Whereas static biases represent time-independent distortions of the vacuum grid, the next section shows that time-dependent transverse shear of the same substrate accounts for the electromagnetic field itself. In this way, VBT unifies the ontology of both static and dynamic electrodynamic phenomena under a single breathing vacuum framework.

8 Electromagnetism as Transverse Shear of the Breathing Vacuum

We model the vacuum as an elastic, isotropic medium. The global Planck-rate breathing is a *longitudinal, conformal* modulation (Section 2), while electromagnetism arises from *transverse shear* excitations on top of that breathing. Denote by $\boldsymbol{\xi}_\perp(\mathbf{x}, t)$ the small transverse displacement of the vacuum fabric, with effective mass density ρ_v and shear stiffness κ_v (both defined after Planck-time averaging).

8.1 Wave Equation and Light Speed

Small-amplitude transverse deformations obey the linear elastic wave equation

$$\rho_v\,\partial_t^2\boldsymbol{\xi}_\perp - \kappa_v\,\nabla^2\boldsymbol{\xi}_\perp = 0, \qquad c^2 \equiv \frac{\kappa_v}{\rho_v}. \tag{52}$$

Thus, shear waves propagate at the universal speed c, fixed by the vacuum's elastic constants. Because the Planck breathing is conformal, null cones are preserved under the average, and Eq. (52) is Lorentz-covariant at low frequencies ($\omega \ll \omega_P$).

8.2 Gauge Potentials and Fields

Define electromagnetic potentials as linear functionals of the transverse displacement (choosing a convenient normalization Λ):

$$\mathbf{A} \equiv \Lambda\, \partial_t \boldsymbol{\xi}_\perp, \qquad \phi \equiv -\,\Lambda\, c^2\, \nabla\cdot\boldsymbol{\xi}_\parallel, \tag{53}$$

and the usual fields

$$\mathbf{E} = -\nabla\phi - \partial_t \mathbf{A}, \qquad \mathbf{B} = \nabla \times \mathbf{A}. \tag{54}$$

A relabeling of the microscopic carrier phase (Sec. §2) corresponds to $\boldsymbol{\xi}_\perp \mapsto \boldsymbol{\xi}_\perp + \nabla\chi$ at fixed $\partial_t \boldsymbol{\xi}_\perp$, yielding the familiar $U(1)$ gauge freedom $\mathbf{A} \mapsto \mathbf{A} + \nabla\chi,\ \phi \mapsto \phi - \partial_t\chi$.

8.3 Maxwell's Equations (Coarse-Grained)

After Planck-time averaging and in the linear regime, $\mathbf{E}, \mathbf{B}$ obey Maxwell's equations in vacuum,

$$\begin{aligned} \nabla\cdot\mathbf{E} &= \frac{\rho}{\varepsilon_0}, \qquad & \nabla\times\mathbf{B} - \frac{1}{c^2}\,\partial_t\mathbf{E} &= \mu_0\,\mathbf{J}, \\ \nabla\cdot\mathbf{B} &= 0, & \nabla\times\mathbf{E} + \partial_t\mathbf{B} &= 0, \end{aligned} \tag{55}$$

with constitutive parameters determined by the vacuum's elastic constants. Up to an overall normalization (set by measurements of c and Z_0),

$$c^2 = \frac{1}{\varepsilon_0\mu_0} = \frac{\kappa_v}{\rho_v}, \qquad Z_0 \equiv \sqrt{\frac{\mu_0}{\varepsilon_0}} \;\propto\; \sqrt{\frac{1}{\kappa_v\,\rho_v}}. \tag{56}$$

Different choices of Λ rescale (ε_0, μ_0) together while leaving c invariant; Z_0 fixes the remaining normalization.

8.4 Coupling to Matter (Minimal Coupling)

A matter envelope $A(\mathbf{x}, t)$ (Section 3) phase-locks weakly to the carrier. Slow transverse twists of the vacuum change the local beat phase $\varphi \mapsto \varphi - (q/\hbar)\chi$, enforcing the covariant derivative

$$\partial_\mu \;\longrightarrow\; D_\mu \equiv \partial_\mu - i\,\frac{q}{\hbar}\,A_\mu, \qquad A_\mu = \left(\frac{\phi}{c},\, \mathbf{A}\right), \tag{57}$$

and yielding the standard Schrödinger/Pauli/Dirac couplings to the electromagnetic field. Gauge invariance of the matter action gives the continuity equation $\partial_t\rho + \nabla\cdot\mathbf{J} = 0$ by Noether's theorem.

8.5 Photons and Lorentz Symmetry

Quanta of $\boldsymbol{\xi}_\perp$ are the photons. Because the Planck-rate breathing enters only as a conformal factor, the coarse-grained photon dynamics are strictly null ($ds^2 = 0$) and Lorentz symmetry remains intact to all orders in ω/ω_P at the linear level. Any residual Planck-scale imprints must be higher-order, suppressed by powers of $\omega/\omega_P \ll 1$.

9 Gravity in the Breathing Vacuum

9.1 A_{mean} as Curvature

In General Relativity, gravitation is explained as the curvature of spacetime [4, 41]. In VBT, curvature emerges instead as a local suppression of the vacuum breathing amplitude. Let A_{mean} denote the midpoint (zero crossing) of the Planck-scale oscillation. In free space this is spatially uniform. When mass-energy is present, the local breathing amplitude is reduced, shifting A_{mean} downward. Observers living at the zero crossing perceive this as gravitational curvature.

Interpretation. In VBT gravitation is encoded purely as amplitude suppression of the global breathing ($\alpha(\mathbf{x})$). The Planck-frequency carrier itself remains globally synchronized; there are no local phase offsets. Thus spacetime curvature corresponds to a downward shift of A_{mean}, not to regional desynchronization of the vacuum oscillation.

9.2 Weak-Field Limit

To make contact with experiment, we examine the weak-field limit. Consider a metric ansatz

$$ds^2 = A(x)^2 c^2 dt^2 - A(x)^{-2} dx^2, \quad A(x) = e^{\Phi(x)/c^2}, \tag{58}$$

where $\Phi(\mathbf{x})$ is an effective potential determined by the suppressed amplitude. Expanding to first order yields

$$g_{00} \approx 1 + 2\Phi/c^2, \quad g_{ij} \approx -(1 - 2\Phi/c^2)\delta_{ij},$$

reproducing the standard weak-field metric of GR. Expanding $ds^2 = A(\mathbf{x})^2 c^2 dt^2 - A(\mathbf{x})^{-2} d\mathbf{x}^2$ with $A = e^{\Phi/c^2}$ to $\mathcal{O}(\Phi/c^2)$ gives $g_{00} = 1 + 2\Phi/c^2$ and $g_{ij} = -(1 - 2\Phi/c^2)\delta_{ij}$, corresponding to PPN parameters $\gamma = \beta = 1$ at this order. The weak-field metric recovers light deflection, perihelion precession, and time delay consistent with PPN parameters [42].

In the weak-field limit the breathing midpoint reproduces the familiar post-Newtonian parameters $\gamma = \beta = 1$, and as shown in Appendix F this construction yields the correct deflection of light and gravitational redshift. Thus the geometric reinterpretation remains consistent with all solar-system tests of general relativity.

9.3 Observable Tests

This weak-field form reproduces classical tests of gravity:

- *Newtonian limit:* $\nabla^2\Phi = 4\pi G\rho$ matches Poisson's equation, with G identified as the coupling constant [37].
- *Gravitational redshift:* Clocks deeper in a suppressed A_{mean} run slower, in agreement with Pound–Rebka and later precision measurements.
- *Light bending:* Photons follow null geodesics in the metric above, giving deflection angle $\Delta\phi = 4GM/(c^2 b)$, matching GR's prediction and Eddington's eclipse result.
- *Time delay:* Radar signals grazing the Sun accumulate extra delay (Shapiro effect), again reproduced by the weak-field metric form.

9.4 Interpretation

Thus VBT interprets gravitation as an amplitude effect rather than a phase effect: the breathing itself remains globally synchronized, but local suppression of its midpoint shifts spacetime geometry. The formalism is consistent with General Relativity in the weak field while offering a different ontological interpretation: spacetime curvature emerges from vacuum breathing amplitude, not intrinsic geometry. Further details on gravity math bridge are provided in Appendix E and Appendix F.

9.5 Future Work

The present development has focused on the weak-field regime, where the expansion of the breathing midpoint reproduces the PPN parameters $\gamma = \beta = 1$ consistent with general relativity. A natural next step is to extend the analysis into the strong-field domain. In particular, the question of whether VBT admits horizon-like structures analogous to those of black holes in general relativity remains open. Because the breathing amplitude never strictly vanishes, it is plausible that singular horizons are replaced by limiting states with finite oscillatory support. A full treatment of this regime is left for future work, but the weak-field agreement ensures consistency with all current solar-system tests of gravity.

10 Cosmology in the Vacuum Breathing Theory

10.1 The Expanding Vacuum

In the Vacuum Breathing Theory (VBT), cosmology is reinterpreted as a consequence of how the breathing vacuum evolves on the largest scales. While local gravitational effects are described by suppression of A_{mean}, the universe as a whole is governed by a slow, cumulative shift in the breathing field across cosmic distances.

10.2 Redshift and redshift drift

In conventional cosmology, redshift is attributed to metric expansion of space, with the observed drift in redshift over time (the Sandage–Loeb effect) given by

$$\frac{dz}{dt_0} = (1+z)H_0 - H(z), \tag{59}$$

where $H(z)$ is the Hubble parameter and t_0 is the observer's proper time. This predicts a characteristic signature: the drift is negative at low z ($\lesssim 2$) and becomes positive at higher z.

In the VBT framework, redshift arises instead from evolution of the mean breathing amplitude $A_{\text{mean}}(t)$. A photon emitted at epoch t_e and observed at t_0 is redshifted by

$$1 + z = \frac{A_{\text{mean}}(t_0)}{A_{\text{mean}}(t_e)}. \tag{60}$$

Differentiating with respect to the observer's time yields

$$\frac{dz}{dt_0} = \frac{\dot{A}_{\text{mean}}(t_0)}{A_{\text{mean}}(t_e)} - \frac{\dot{A}_{\text{mean}}(t_e)}{A_{\text{mean}}(t_e)}\frac{dt_e}{dt_0}. \tag{61}$$

The precise form depends on the time dependence of A_{mean}, but in general the drift is monotonic: its sign is set by whether $A_{\text{mean}}(t)$ increases or decreases with cosmic time.

A direct corollary is the time-dilation of light curves. In VBT, the observed broadening of supernova or quasar light curves by a factor $(1 + z)$ follows immediately from the same amplitude scaling that governs spectral redshift. Thus the light-curve stretching and photon frequency shift are unified as two manifestations of the evolving vacuum carrier.

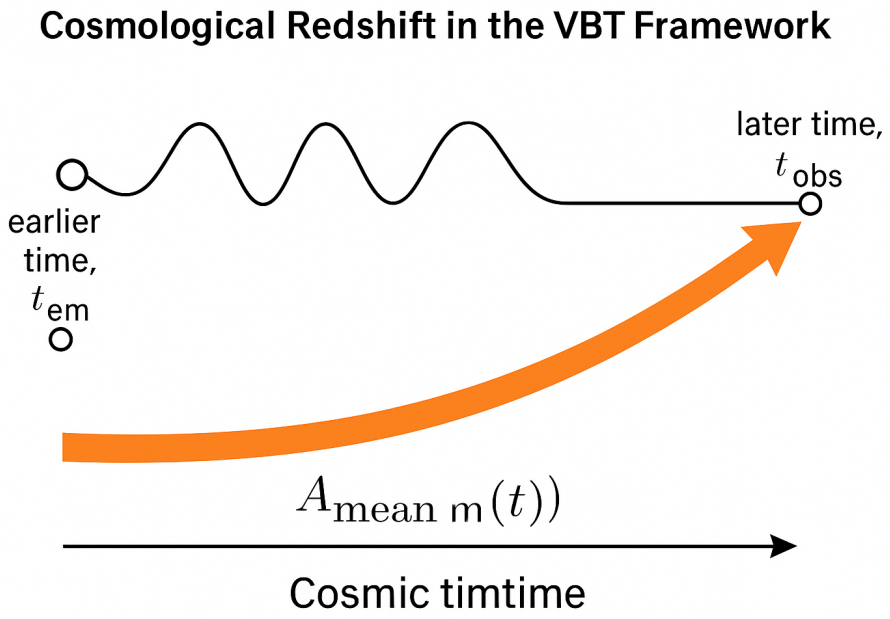

Figure 15: **Comparison of redshift drift.** ΛCDM (solid curve) predicts a sign change in $\dot{z}$ between low and high redshift. VBT (dashed curve) predicts a monotonic drift set by the time derivative of A_{mean}, with no sign reversal. Measurement of the drift sign therefore provides a direct observational test of the theory.

This distinction provides a falsifiable prediction: ΛCDM requires a sign change in $\dot{z}$ between low and high redshift, while VBT predicts a consistent sign across all epochs (Fig. 15). Long-baseline spectroscopic programs with next-generation instruments (e.g. ELT, high-resolution quasar surveys) can therefore discriminate between the two pictures by measuring whether the redshift drift ever changes sign.

10.3 The Cosmic Microwave Background

The Cosmic Microwave Background (CMB) is interpreted in ΛCDM as relic radiation from recombination, with a nearly perfect blackbody spectrum. In VBT, the CMB arises as the frozen residue of early-universe synchronization of the vacuum breathing. Tiny fluctuations in amplitude A_{mean} imprint the observed anisotropies. The Planck 2018 results [6] provide tight observational constraints, which VBT must satisfy: power-spectrum peaks correspond to standing-wave modulations of the breathing fabric at recombination. A quantitative fit to the TT/TE/EE spectra and BAO is deferred to future work; the present discussion is limited to the qualitative mapping between amplitude fluctuations and acoustic peaks.

10.4 Large-Scale Structure and Dark Components

Standard cosmology invokes dark matter and dark energy to explain galactic rotation curves and cosmic acceleration. VBT offers an alternative: long-range suppression of A_{mean} by the population of stellar-mass black holes distributed across galaxies. The cumulative effect produces the upward bias in galactic rotation without requiring non-baryonic dark matter. Similarly, cosmic acceleration may reflect global relaxation of breathing amplitude rather than a separate dark-energy field. We note that attributing galactic rotation support to a distributed population of stellar-mass black holes is subject to strong microlensing constraints [43, 44]; here we treat this as a working hypothesis for how cumulative A_{mean} suppression might arise, but the relationship with dark matter remains an open hypothesis under investigation.

While the breathing-vacuum framework provides a natural account of cosmological redshift and the CMB reference state, the explanation of galactic rotation curves remains an open question. A plausible direction, explored in earlier drafts, is that the statistical distribution of stellar-mass black holes may collectively bias the vacuum fabric to mimic the effects attributed to dark matter. This possibility remains speculative and is left for future development, but is included here to highlight one possible pathway toward a full cosmological model.

10.5 Interpretation

VBT thus provides a cosmological framework grounded in the same vacuum dynamics that explain atomic and gravitational phenomena. Redshift, the CMB, and structure formation are unified in terms of the breathing vacuum, which serves as the universal medium for both microphysics and cosmic evolution. Quantitative confrontation with Planck data remains future work, but the framework offers a coherent reinterpretation of cosmological observables.

.

11 Observables

A central strength of the Vacuum Breathing Theory (VBT) is that it not only offers a coherent framework for unifying fundamental interactions, but also connects directly to experimental observables. Several known phenomena that, in conventional quantum field theory, are explained through virtual particle exchange or perturbative effects, emerge naturally within the VBT as direct manifestations of the breathing vacuum. In this section we outline key examples.

11.1 Faraday Effect

The Faraday effect, discovered in 1846 [45], shows that the polarization of light is rotated when propagating through a medium subjected to a static magnetic field. In conventional electrodynamics this arises from magneto-optical coupling of the medium. In VBT, the interpretation is more direct: the static torsional bias (magnetic field) locally alters the orientation of the vacuum grid. A propagating electromagnetic wave experiences a slow twist in its polarization vector as it rides the breathing fabric, producing the observed rotation.

11.2 Kerr Effect

The Kerr effect, reported in 1875 [46], demonstrates that a static electric field can alter the polarization state of light in a dielectric. Analogous to the Faraday effect, VBT interprets this as the influence of a radial bias on the breathing grid. A photon traveling through the region is slightly

phase-shifted between field directions aligned and perpendicular to the bias, producing birefringence. Both Faraday and Kerr thus emerge from static vacuum biases acting on the Planck-scale oscillation, without need for additional exchange particles.

11.3 Casimir Effect

The Casimir effect, first predicted in 1948 [47] and later experimentally confirmed [48, 49], is often described in terms of vacuum zero-point fluctuations. Two conducting plates placed microns apart experience a measurable force of attraction due to mode suppression between them as illustrated in Figure 16. In VBT, this arises instead as an interpolation effect: the breathing grid between plates is constrained by boundary conditions, leading to a net inward bias. The observed force is then a geometric consequence of the oscillating vacuum fabric, consistent with measured magnitudes.

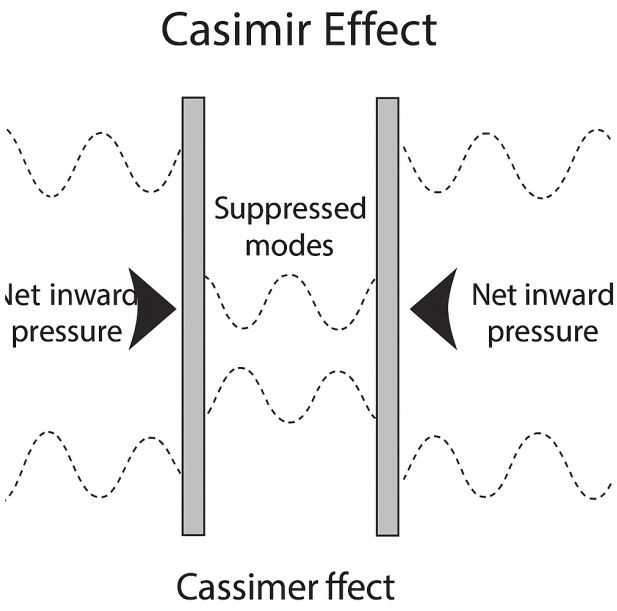

Figure 16: Conducting plates constrain vacuum breathing modes, reducing A_{mean} oscillatory states between the plates and producing a net attractive force.

In this framework, the Casimir effect is not mediated by hypothetical virtual photons but arises directly from the geometric-dependent modulation of A_{mean}. As the plates approach one another, the breathing cycles of the vacuum are constrained, reducing the number of supported oscillatory states. The result is a measurable force that follows the well-known $1/d^4$ scaling with separation distance d. Finite conductivity, temperature, and material-response corrections enter as modified boundary conditions in this picture, reproducing the known deviations from the ideal $1/d^4$ law. VBT interprets this as a natural consequence of the vacuum breathing amplitude acting as the universal carrier of forces. The Casimir effect thus provides a striking observable confirmation of the VBT framework, highlighting how even static, charge-neutral systems can interact through the structured breathing of the vacuum field.

11.4 Spectroscopic Benchmarks

VBT must also reproduce the highly precise benchmarks of atomic spectroscopy. For hydrogen, the $1S$–$2S$ interval and Lamb shift are among the most sensitive tests. In VBT, the Lamb shift

appears naturally as a small contact-like correction due to precession in the s-orbitals (Sec. 4). Likewise, the $2p \to 1s$ spontaneous emission rate calculated in Sec. 4 agrees with the tabulated Einstein A-coefficient from the NIST database [50], showing that photon emission arises correctly from re-locking of the orbital phase. Beyond the intrinsic spectral benchmarks, external-field perturbations provide an additional test of the VBT framework. In conventional quantum mechanics, the magnetic quantum number m labels the orientation of orbital angular momentum relative to an applied field axis, giving rise to Zeeman splitting. In VBT this effect is reinterpreted geometrically: a torsional bias of the vacuum grid (magnetic field) establishes a preferred axis, and the electron's shuttle precession locks into discrete orientation states relative to it. These correspond to the allowed m values, with the observed spectral splitting arising directly from the geometric interaction between orbital precession and the torsional bias. This links the orbital dynamics described in Section 4 with the static-bias picture of Section 7, providing a coherent account of spectroscopic splitting phenomena.

11.5 Fine structure and spin–orbit coupling.

Another spectroscopic consequence of angular momentum in atoms is the fine-structure splitting, conventionally attributed to spin–orbit coupling. In the VBT framework, this arises naturally from the interaction between the electron's intrinsic loop chirality (spin) and the orbital precession within its own Coulomb-induced torsional bias. The standing-wave loop that defines the electron can phase-lock in two chiral senses, $s = \frac{1}{2}$, which interact differently with the local vacuum twist generated by orbital motion. The result is a small shift of the energy levels, analogous to conventional spin–orbit coupling, but here reinterpreted as a geometric interaction between spin chirality and orbital precession within the breathing substrate. Thus, both Zeeman and fine-structure splittings are accounted for in VBT as direct manifestations of how orbital and spin degrees of freedom couple to radial and torsional biases of the vacuum grid.

Our contact-like precession model captures the correct n and Z trends qualitatively but is not a replacement for QED radiative corrections; a full magnitude calculation is left for future work.

11.6 Summary

The Faraday and Kerr effects, usually derived within the framework of classical wave optics, are here interpreted in VBT as static biases. These effects serve as observational anchors for the breathing vacuum. Rather than invoking separate phenomena, VBT provides a single geometric substrate: static biases of the vacuum grid alter polarization; boundary conditions generate Casimir forces; and orbital phase-locking dictates spectroscopic transitions. Together these results demonstrate that VBT is not only mathematically self-consistent but also experimentally grounded.

12 Speculative Mapping to the Standard Model

12.1 Status and Motivation

The following discussion is *heuristic and conjectural*. It is not a full derivation of the Standard Model from VBT, but rather a working hypothesis for how vacuum configurations in the breathing fabric may correspond to known degrees of freedom. The aim is to show that the **structural language** of VBT naturally mirrors key features of fermions, gauge bosons, and the Higgs sector.

The idea of quantized structures resembling knots and vortices dates back to Helmholtz's original work on vortex dynamics [32], which provides historical context for these heuristic mappings.

12.2 Knots as Fermions

Localized knotted configurations of the breathing fabric may be identified with fermionic matter. The conserved *topological charge* of such a configuration serves as an analogue of baryon or lepton number. For example, a Chern–Pontryagin index of the form

$$Q_{\text{top}} \;=\; \frac{1}{32\pi^2}\int \epsilon^{\mu\nu\rho\sigma}\, F_{\mu\nu}F_{\rho\sigma}\, d^4x \tag{62}$$

is quantized and conserved, suggesting that knot number plays the role of a fermion count. The stability of electron- or proton-like states then follows from the nontrivial topology of the vacuum knots.

12.3 Torsional Links as Gauge Bosons

A torsional bias in the vacuum grid resembles a gauge connection. Promoting the torsional fields to a non–Abelian structure yields curvatures of the form

$$G^a_{\mu\nu} \;=\; \partial_\mu A^a_\nu - \partial_\nu A^a_\mu + f^{abc}A^b_\mu A^c_\nu, \tag{63}$$

the standard Yang–Mills field strength. In this picture, gluons (and more generally gauge bosons) emerge as quanta of torsional excitations in the vacuum fabric.

12.4 Higgs Analogy

A nonzero mean amplitude of the breathing field plays the role of a vacuum expectation value:

$$\langle A(t)\rangle \;=\; A_{\text{mean}} \;\neq\; 0. \tag{64}$$

This offset sets effective inertial scales and couples to knot states, analogous to how the Higgs field endows particles with mass in the Standard Model.

12.5 Summary Table

The speculative correspondences may be summarized as:

VBT construct	**Standard Model analogue**
Knotted vacuum configuration	Fermion (electron, quark, proton)
Torsional link / bias	Gauge boson (gluons, W, Z, photon)
Nonzero mean breathing amplitude A_{mean}	Higgs vacuum expectation value

12.6 Future Work

At present this mapping is schematic. We have shown that radial and torsional biases generate Coulomb- and Biot–Savart–like fields, and that knots can carry conserved charges. To extend this framework into a full Standard Model embedding, one would need to construct explicit non–Abelian gauge structures within the vacuum lattice, classify distinct knot families, and show how three fermion generations and mixing arise. These steps are beyond the present work, but define a concrete path forward.

13 Discussion

The Vacuum Breathing Theory (VBT) offers a framework in which multiple long-standing puzzles of quantum mechanics emerge naturally from the dynamics of the vacuum fabric. A central insight is that all matter is built from closed standing-wave configurations of the vacuum oscillation, with A_{mean} defining the spacetime "zero crossing" in which physical reality resides. Within this framework, phenomena often treated as fundamentally mysterious can be reframed in a direct physical manner.

13.1 Entanglement as Vacuum Synchronization

In VBT, entanglement correlations are attributed to shared phase histories written into the breathing vacuum at interaction, yielding non-signaling correlations without superluminal communication. This account is explicitly compatible with experimental violations of Bell inequalities; it does not restore local hidden variables but frames the correlations as arising from common vacuum-phase constraints rather than dynamical signals.

13.2 Double-Slit Interference

The double-slit experiment remains a touchstone for wave–particle duality. In VBT, the explanation is straightforward: every quantum entity is a standing wave on the breathing vacuum. Passage through both slits corresponds to two coherent paths of the same envelope on the Planck carrier. The interference pattern is the direct manifestation of vacuum modulation, not a paradox of "particle deciding path." Collapse upon detection reflects the re-locking of the standing wave to a specific localized oscillation of the fabric. Thus, wave–particle duality becomes a natural consequence of the carrier–envelope framework.

13.3 Interpretive Scope

These examples illustrate how VBT reframes some of the most puzzling quantum phenomena without additional postulates. Entanglement follows from global synchronization of the breathing fabric; interference arises from the wave nature of all excitations; uncertainty (Sec. 3) emerges as a carrier–envelope constraint. Together, these interpretations suggest that the breathing vacuum provides a unifying ontological substrate for both quantum mechanics and relativity.

14 Conclusion and Outlook

The Vacuum Breathing Theory (VBT)[11] reframes atomic and quantum dynamics as deterministic phase-locking to a universal vacuum oscillation. In place of stochastic jumps or purely abstract symmetry arguments, VBT introduces a physical mechanism: inertia, transition delays, and apparent randomness all emerge from the degree of mismatch between local oscillations and the breathing of the vacuum.

14.1 Summary of Achievements

- **Atomic transitions:** VBT provides a continuous description of electron orbital changes, reproducing hydrogen spectral lines without relying on discontinuous quantum jumps. The Lamb shift is reinterpreted as a modulation of vacuum phase-locking, not random vacuum fluctuations.

- **Photon emission:** Whereas QED assumes exponential spontaneous decay, VBT predicts finite, delayed photon wavepackets whose causal onset scales with coupling parameters. This yields measurable departures from the purely memoryless exponential law in single-photon time-correlated experiments.
- **Massless quasiparticles:** Dirac fermions in graphene and massless excitons in hBN are explained as cases where phase mismatch to the vacuum vanishes, eliminating effective mass. VBT therefore unifies atomic inertia and emergent condensed-matter anomalies within the same framework.
- **Tunneling:** The paradox of instantaneous or undefined tunneling times is replaced by a deterministic account. VBT adds finite re-locking delays at barrier interfaces on top of the Büttiker–Landauer dwell, producing causal, tunable corrections in the attosecond regime.

14.2 Falsifiable Predictions

VBT is falsifiable by multiple, independent experimental probes:

1. **Orbital transitions:** Continuous energy–time trajectories predict specific spectral envelopes. Observation of strictly discontinuous behavior would contradict VBT.
2. **Photon emission:** Single-photon time-correlated histograms should reveal causal onsets and finite packet envelopes, not perfect exponentials. The predicted delay scales with Ω/α and should be tunable.
3. **Lamb shift:** Residuals in precision spectroscopy should scale with S-state wavefunction density $\propto 1/n^3$. Absence of such a systematic trend would falsify this aspect of VBT.
4. **Massless quasiparticles:** Effective masslessness should be tunable by strain, dielectric environment, or applied fields. If massless points prove fixed and untunable, VBT's coupling interpretation fails.
5. **Tunneling times:** Attosecond measurements should show a positive, finite excess delay over τ_{BL}, scaling with interface gradient and coupling strength. Observation of strictly memoryless exponential decay with no tunable delay falsifies VBT.

14.3 Outlook

Together these predictions define a program of near-term experimental tests. Attosecond streaking can probe tunneling delays, single-photon sources with TCSPC can test emission envelopes, and precision spectroscopy can check S-state scaling. Condensed-matter experiments on graphene and hBN provide a bridge to quantum materials. In all cases the VBT predictions are concrete, causal, and testable. Either confirmation or falsification will advance our understanding of whether vacuum breathing is a true foundation of quantum physics. In addition to astrophysical signatures such as redshift scaling, laboratory tests are possible. A concrete proposal for probing the temporal structure of single-photon emission with trapped ions provides a direct falsification pathway for the VBT framework [7].

Glossary

A_{local} The local breathing amplitude, representing deviations in the vacuum near mass-energy concentrations. It defines how the grid oscillates relative to the cosmic reference state A_{mean}.
A_{mean} The cycle-averaged amplitude of the breathing vacuum. This dimensionless parameter defines the reference state of spacetime and is tied to cosmic evolution. Laboratory rulers and clocks are implicitly calibrated to A_{mean}.
Apparent Speed ($\dot{r}$) The velocity of an electron or wavepacket measured in laboratory coordinates. Apparent speed varies because of the breathing factor $a(t)$, even when motion through the fabric is uniform.
Breathing Amplitude (ε) The fractional modulation of space per Planck cycle. Defined such that one full peak-to-peak oscillation corresponds to one Planck length per Planck length.
Breathing Factor ($a(t)$) The instantaneous scaling factor relating the comoving (fabric) coordinate χ to the physical radius $r(t)$: $r(t) = a(t)\chi(t)$.
Breathing Phase (u) A normalized parameter $u \in [0, 1]$ describing progress within one breathing cycle, used to schedule electron motion and inverse-CDF sampling of radial probability densities.
Carrier Phase (Φ_P) The rapid Planck-frequency oscillation of the vacuum fabric. Serves as the universal reference clock on which slower matter-wave envelopes are imposed.
Comoving / Fabric Coordinate (χ) The coordinate that moves with the breathing vacuum. Motion at constant $|\dot{\chi}|$ is non-radiating, even though the apparent lab-frame motion may oscillate.
Diametric Shuttle The motion assigned to s-orbitals (e.g., hydrogen 1s, 2s) in VBT: back-and-forth passes through the nucleus along nearly diametric lines, with azimuthal updates between cycles to restore isotropy.
Dwell Probability The effective time spent near a given radius in orbital motion. At orbital nodes, the dwell probability tends to zero, ensuring smooth transit rather than reflection.
Envelope (A) The slowly varying amplitude of a matter wave riding on the Planck carrier. Determines probability densities and obeys the Schrödinger equation after averaging over the fast oscillation.
Factor-of-Two Modulation The requirement that the Coulomb potential experienced by an electron be modulated such that its orbital radius oscillates between $r_0/2$ and $2r_0$ during each cycle. This ensures the virial theorem and reproduces the hydrogen 1s probability density.
Fabric Frame The reference frame comoving with the breathing vacuum, in which particle speed $|\dot{\chi}|$ is constant and radiation is absent. Contrasts with the lab frame, where apparent speeds oscillate.
Inverse-CDF Construction A numerical technique used to generate electron radial motion consistent with quantum-mechanical probability densities $P_{nl}(r)$. By mapping uniform breathing phase u to radius via the inverse cumulative distribution, exact reproduction of quantum radial distributions is achieved.
Knot Closed standing-wave configurations of the vacuum oscillation, representing particles such as electrons (complete knots), neutrinos (partial knots), and quarks (fractional phase-locked knots).
κ_v The effective shear stiffness of the vacuum substrate. Together with ρ_v it defines the wave speed $c^2 = \kappa_v/\rho_v$. Like ρ_v, it is an emergent property of the breathing vacuum rather than an independent constant of nature. At cosmological scales, κ_v may also co-vary with A_{mean}.
Loop Frequency (f_C) The Compton frequency of a closed electron loop at rest, defined by $f_C = m_e c^2/h$. Interpreted in VBT as a large integer subdivision of the Planck frequency.
Phase-Locking Resonant synchronization between the electron's de Broglie frequency and the vacuum's breathing. Ensures stationarity of atomic orbitals and underlies spectroscopic stability.
Precession ($\delta\theta$) A tiny azimuthal increment added between diametric shuttles. Arises from near-nucleus asymmetries and ensures isotropy without imparting net angular momentum.

$\boldsymbol{\rho_v}$ The effective mass density of the vacuum substrate. It appears in the elastic analogy (Sec. 6) alongside κ_v, with the wave speed given by $c^2 = \kappa_v/\rho_v$. It is not a new fundamental constant but an emergent parameter of the breathing vacuum. At cosmological scales, ρ_v may co-vary with the cycle-averaged amplitude A_{mean}.
Radial Bias A static outward (positive charge) or inward (negative charge) displacement of the vacuum grid. Produces electrostatic fields with inverse-square law behavior.
Torsional Bias A static twist of the vacuum grid corresponding to magnetism. Produces azimuthal field lines looping from pole to pole.
Vacuum Grid The notional lattice of points representing the breathing spacetime fabric. Local radial or torsional biases of this grid correspond to charges and magnetic fields.
$f_{\mathbf{orb}}$ — orbital frequency of the electron in its bound state trajectory (Sec. 4.2).
f_b — vacuum breathing frequency; the high-frequency oscillation of the isotropic background fabric (Sec. 4.2).
L^2 — orbital angular momentum operator, eigenvalues $\ell(\ell+1)\hbar^2$ for quantum number ℓ.
L_z — z-component of orbital angular momentum, eigenvalues $m\hbar$ for magnetic quantum number m.
$\Phi_P(t)$ – The global Planck-carrier phase $\Phi_P(t) = \omega_P t$, perfectly synchronized across the universe.
$\varphi(x,t)$ – Envelope phase of a matter wave, spatially varying and responsible for momentum/energy relations. Distinct from Φ_P.
$\theta_{U(1)}(\mathbf{x})$ – Internal order parameter describing topological winding (charge).

Appendices

A Higher hydrogenic states example ($3d_{z^2}$)

Example of a Higher Hydrogenic State ($3d_{z^2}$)

This appendix illustrates how higher hydrogenic statises emerge naturally from the analytic framework of Sec. 4.4, and shows how numerical validation confirms their expected structure.

A.1 Analytic form.

The radial function for the $3d$ state ($n = 3$, $\ell = 2$) is

$$R_{32}(r) = \frac{1}{81\sqrt{30}}\, a_0^{-3/2} \left(\frac{r}{a_0}\right)^2 \exp\!\left(-\tfrac{r}{3a_0}\right), \tag{A.1}$$

with angular dependence given by the spherical harmonic $Y_{20}(\theta,\phi) = \frac{1}{4}\sqrt{\frac{5}{\pi}}(3\cos^2\theta - 1)$. The resulting probability density $P(r,\theta,\phi) = |R_{32}(r)|^2 |Y_{20}(\theta,\phi)|^2$ has the familiar nodal surfaces: two radial nodes and an angular node.

A.2 Numerical validation.

To check consistency, synthetic trajectories were generated with the inverse-CDF method described in Appendix H, and histograms were compared with the analytic densities. The method is used here solely as a *validation tool*: it reproduces the analytic weighting but does not constitute an independent derivation.

- **Radial PDF match:** The histogram of $r(t)$ agrees with the analytic $|R_{32}(r)|^2 r^2$ on $[0, 20a_0]$ with L_1 error $\lesssim 10^{-2}$.
- **Angular PDF match:** The histogram of polar angles matches $|Y_{20}(\theta, \phi)|^2$ to within 10^{-2} in L_1 norm.
- **Angular momentum:** From the synthetic trajectory, $L^2 \simeq 6\hbar^2$ and $L_z \simeq 0$, consistent with $\ell = 2$, $m = 0$.

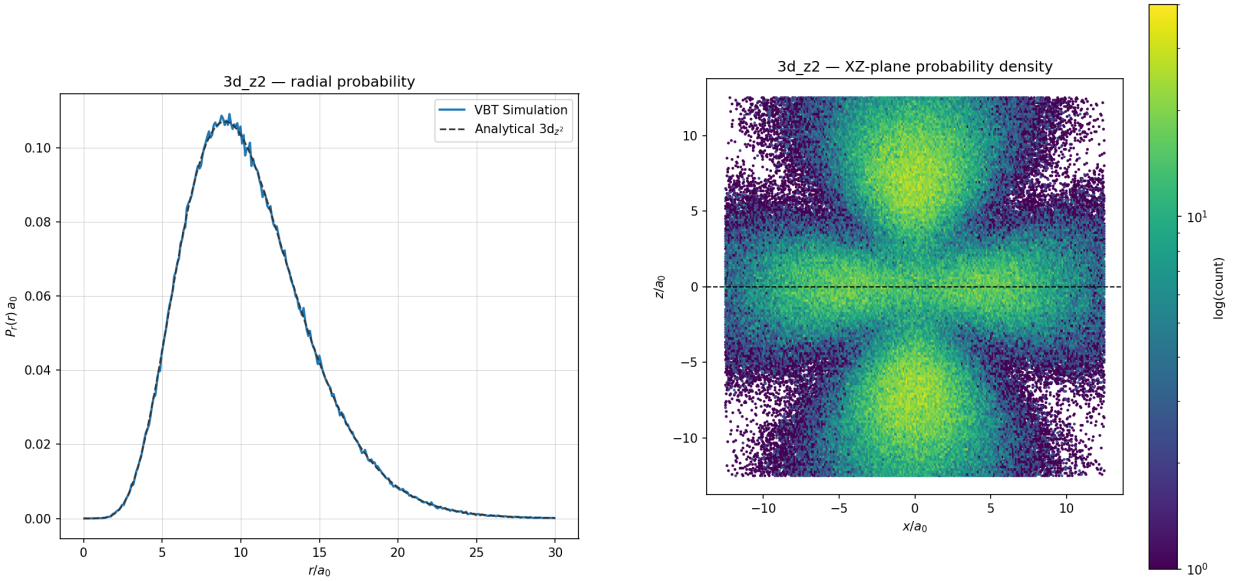

(a) Radial probability density

(b) XZ-plane probability density

Figure 17: **Validation of the $3d_{z^2}$ orbital.** (a) Radial probability histogram from inverse-CDF validation compared with the analytic $|R_{32}(r)|^2 r^2$, confirming the expected radial structure. (b) XZ-plane probability density from inverse-CDF validation, showing the lobes and nodal planes of the $3d_{z^2}$ orbital in agreement with the analytic angular form $|Y_{20}(\theta, \phi)|^2$. Together these results confirm that the VBT sampling reproduces both radial and angular features of the $3d_{z^2}$ state.

A.3 Conclusion.

The $3d_{z^2}$ example illustrates that higher-ℓ orbitals follow straightforwardly from the analytic derivation in Sec. 4.4. Numerical validation confirms the expected radial and angular structure. The main text focuses on $1s$, $2s$, and $2p$ as representative cases; this appendix is included for completeness and intuition.

B Averaged Dynamics and Derived Radial Distributions

B.1 Setup and multiple-scales averaging

Let the physical radius be $r(t) = a(t)\,\chi(t)$, where χ is the comoving (fabric) coordinate and $a(t) = 1 + \varepsilon \cos(\omega_P t)$ is the isotropic breathing factor ($\varepsilon \ll 1$). For a central Coulomb potential

$V(r) = -k/r$ (with $k = k_e e^2$), write the Lagrangian in χ:

$$\begin{aligned} L(\chi, \dot{\chi}, t) &= \frac{m}{2}\left(\dot{a}\,\chi + a\,\dot{\chi}\right)^2 - \left(-\frac{k}{a\,\chi}\right) \\ &= \frac{m}{2}\left(\dot{a}\,\chi + a\,\dot{\chi}\right)^2 + \frac{k}{a\,\chi}\,. \end{aligned} \tag{B.1}$$

Introduce fast and slow times $t_1 = \omega_P t$ and $t_0 = t$, and average over a breathing cycle keeping $\mathcal{O}(\varepsilon^2)$ terms:

$$\langle a^2 \rangle = 1 + \tfrac{1}{2}\varepsilon^2, \qquad \langle a\,\dot{a} \rangle = 0, \qquad \langle \dot{a}^2 \rangle = \tfrac{1}{2}\varepsilon^2\,\omega_P^2, \qquad \left\langle \frac{1}{a} \right\rangle = 1 + \tfrac{1}{2}\varepsilon^2 + \mathcal{O}(\varepsilon^4). \tag{B.2}$$

The cycle-averaged (slow) Lagrangian is

$$L_{\text{eff}}(\chi, \dot{\chi}) \;=\; \frac{m}{2}\,\langle a^2 \rangle\,\dot{\chi}^2 + \frac{m}{2}\,\langle \dot{a}^2 \rangle\,\chi^2 + \frac{k}{\chi}\left\langle \frac{1}{a} \right\rangle. \tag{B.3}$$

Defining $m_* \equiv m\,\langle a^2 \rangle$ and $\Omega^2 \equiv \langle \dot{a}^2 \rangle$, the effective Hamiltonian reads

$$\begin{aligned} H_{\text{eff}}(\chi, p_\chi) &= \frac{p_\chi^2}{2\,m_*} \;-\; \frac{k_*}{\chi} \;+\; \frac{1}{2}\,m\,\Omega^2\,\chi^2, \\ k_* &\equiv k\left\langle \frac{1}{a} \right\rangle. \end{aligned} \tag{B.4}$$

The quadratic term in χ is $\mathcal{O}(\varepsilon^2\,\omega_P^2)$ and originates purely from the fast metric oscillation. In this construction the averaging is precisely over the fast oscillatory component $\xi(t)$ in Eq. (5), leaving only the smooth mean amplitude $A_{\text{mean}}(t)$.

B.2 Emergent quantum dynamics (Madelung form and $\hbar_{\text{eff}}$)

Consider a compressible ensemble of slow trajectories in phase space (χ, p_χ) with density $\rho(\chi, t)$ and velocity $u(\chi, t) = \dot{\chi}$. The Euler–continuity system implied by H_{eff} contains, besides the Coulomb term $-\partial_\chi(k^*/\chi)$ and the centrifugal barrier (for $\ell > 0$), a dispersive contribution arising from the $\frac{1}{2}m\Omega^2\chi^2$ piece.

Writing $\rho = \psi^2$ and choosing a constant $\hbar_{\text{eff}}$ such that

$$\frac{\hbar_{\text{eff}}^2}{2m^*}\frac{\partial_\chi^2\sqrt{\rho}}{\sqrt{\rho}} \;\equiv\; \tfrac{1}{2}m\Omega^2\chi^2 + (\text{curvature terms}), \tag{B.5}$$

the Euler–continuity system becomes equivalent to the stationary Schrödinger equation in the radial coordinate, with $\hbar_{\text{eff}}$ determined by the microscopic breathing parameters through Ω. For $\ell \geq 0$:

$$-\frac{\hbar_{\text{eff}}^2}{2m^*}\,\frac{d^2u}{dr^2} + \left[-\frac{k}{r} + \frac{\hbar_{\text{eff}}^2\ell(\ell+1)}{2m^*r^2}\right]u \;=\; Eu, \qquad u(r) = rR(r),\; r = a\chi. \tag{B.5}$$

Hence the hydrogenic radial solutions $R_{n\ell}(r)$ and probabilities $P_{n\ell}(r) = 4\pi r^2|R_{n\ell}(r)|^2$ follow directly, without parameter fitting. The inverse–CDF method is retained only as a numerical validation of these analytic forms.

Remarks. (i) This identification is the standard Madelung equivalence: a dispersive term ("quantum pressure") proportional to $\nabla^2\sqrt{\rho}/\sqrt{\rho}$ is dynamically indistinguishable from a microscopic cycle-averaged stiffening; the coefficient defines $\hbar_{\text{eff}}$. (ii) On atomic scales the χ^2 piece is small but crucial for producing the exponential tails of $R_{n\ell}$.

—

B.3 Occupation–time law (distribution directly from dynamics)

For a periodic slow orbit with energy E in the effective central potential

$$V_{\text{eff}}(r) = -\frac{k}{r} + \frac{\hbar_{\text{eff}}^2 \ell(\ell+1)}{2m^* r^2}, \tag{B.6}$$

the time–occupation law gives the radial probability (angle–averaged by uniform precession):

$$P_{n\ell}(r) = N r^2 |v_r(r)|, \quad v_r(r) = \sqrt{\frac{2}{m^*}(E - V_{\text{eff}}(r))} \tag{B.7}$$

Normalizing $\int_0^\infty P_{n\ell}(r)\, dr = 1$ and applying the EBK quantization condition

$$\oint p_r\, dr \;=\; \pi\hbar_{\text{eff}}(2n_r + \ell + 1),$$

yields the discrete spectrum

$$E_n = -\frac{m^* k^2}{2\hbar_{\text{eff}}^2}\,\frac{1}{n^2},$$

and reconstructs the known hydrogenic $P_{n\ell}(r)$.

B.4 Small- and large-r behavior and nodes (diagnostics)

From Eqs.(B.5) or (B.7) it follows that:

- Near $r \to 0$, regularity and the centrifugal barrier give $P_{n\ell}(r) \sim r^{2\ell+2}$ (e.g., r^2 for $1s$, r^4 for $2p$).
- For large r, a turning-point/EBK analysis gives $P_{n\ell}(r) \sim r^2 \exp\!\big(-2r/(na_0)\big)$ with $a_0 = \hbar_{\text{eff}}^2/(m_* k)$.
- The polynomial factor exhibits exactly $n - \ell - 1$ radial nodes (Laguerre structure).

All three features match the quantum-mechanical forms and are derived from dynamics.

C Radiation and Stability in the Conformal Fabric

C.1 Maxwell theory in a conformally flat metric

Let the physical metric be conformally flat,

$$ds^2 \;=\; A(\eta)^2\left(c^2 d\eta^2 - d\boldsymbol{\chi}^2\right), \qquad A(\eta) > 0, \tag{C.1}$$

with conformal time η and comoving spatial coordinates $\boldsymbol{\chi}$. The conformal factor $A(\eta)$ in this setting plays the same role as the cycle-averaged $A_{\text{mean}}(t)$ introduced in Eq. (4), providing the smooth background scale against which oscillations occur. In four spacetime dimensions the *source–free* Maxwell equations are conformally invariant: if $F_{\mu\nu}$ solves $\nabla_\mu F^{\mu\nu} = 0$ and $\nabla_{[\alpha}F_{\beta\gamma]} = 0$ in the metric $g_{\mu\nu} = A^2\eta_{\mu\nu}$, then the rescaled field $\tilde{F}^{\mu\nu} = F^{\mu\nu}$ (indices raised by $\eta_{\mu\nu}$) obeys the flat-space equations $\partial_\mu \tilde{F}^{\mu\nu} = 0$, $\partial_{[\alpha}\tilde{F}_{\beta\gamma]} = 0$ in $(\eta, \boldsymbol{\chi})$. With sources, $\nabla_\mu F^{\mu\nu} = \mu_0 J^\nu$ becomes, after rescaling,

$$\partial_\mu \tilde{F}^{\mu\nu} \;=\; \mu_0\, A^3\, \tilde{J}^\nu, \qquad \tilde{J}^\nu \equiv A^{-3} J^\nu, \tag{C.2}$$

and charge conservation is $\partial_\nu \tilde{J}^\nu = 0$. Thus the field equations in $(\eta, \boldsymbol{\chi})$ take the *Minkowski form* with a conserved current $\tilde{J}^\nu$.

C.2 Poynting flux and conformal scaling

Let $T^{\mu\nu}_{\rm EM} = \frac{1}{\mu_0}\big(F^{\mu\alpha}F^{\nu}{}_{\alpha} - \frac{1}{4}g^{\mu\nu}F^{\alpha\beta}F_{\alpha\beta}\big)$ be the electromagnetic stress–energy tensor. In the conformal metric (C.1) and for any hypersurface with unit normal n_μ and induced area element $d\Sigma_\nu$, the *radiated power* through a large sphere $\mathcal{S}_R$ (radius R in χ–coordinates) is

$$P(\eta) \;=\; \int_{\mathcal{S}_R} T^{\mu\nu}_{\rm EM}\, u_\mu\, d\Sigma_\nu, \qquad u^\mu = A^{-1}(1,\mathbf{0}) \text{ (static observer)}. \tag{C.3}$$

Using the conformal relation and the rescaled (Minkowski) fields $\tilde{\mathbf{E}}, \tilde{\mathbf{B}}$ defined in $(\eta, \boldsymbol{\chi})$, one finds

$$P(\eta) \;=\; A(\eta)^{-4}\,\tilde{P}(\eta), \qquad \tilde{P}(\eta) \equiv \int_{\tilde{\mathcal{S}}_R} \tilde{\mathbf{S}}\cdot d\tilde{\mathbf{A}}, \tag{C.4}$$

where $\tilde{\mathbf{S}} = \frac{1}{\mu_0}\,\tilde{\mathbf{E}}\times\tilde{\mathbf{B}}$ is the flat-space Poynting vector in the $(\eta,\boldsymbol{\chi})$ chart. Thus the question of radiation in the physical metric reduces to whether $\tilde{P}$ is nonzero in the conformal frame. If the cycle–average $\langle\tilde{P}\rangle_\eta = 0$, then $\langle P\rangle = 0$ as well.

C.3 Stationary bound states as standing–wave sources

In VBT, a stationary atomic state corresponds to a *time–periodic and spatially localized* current $\tilde{J}^\mu(\eta,\boldsymbol{\chi})$ in the conformal frame (e.g. the diametric shuttle for s–states, with uniform motion through the fabric between turning regions). Decompose the source in temporal Fourier modes:

$$\tilde{J}^\mu(\eta,\boldsymbol{\chi}) \;=\; \sum_{n\in\mathbb{Z}} \hat{J}^\mu_n(\boldsymbol{\chi})\, e^{-in\omega_b\,\eta}, \qquad \omega_b = \text{breathing/beat frequency}. \tag{C.5}$$

The causal (outgoing-wave) solution in flat $(\eta,\boldsymbol{\chi})$ separates into near- and far-field parts. At large $\chi = R$, the radiative field is proportional to the causal time derivatives of the *multipole moments* of $\hat{J}^\mu_n$. For a *standing-wave* source built from equal–amplitude counter–propagating harmonics (the constructive mechanism for stationarity), the outgoing and incoming $1/R$ pieces cancel in the cycle average:

$$\tilde{\mathbf{E}}^{\rm rad} \;=\; \tilde{\mathbf{E}}^{\rm rad}_{+}+\tilde{\mathbf{E}}^{\rm rad}_{-}, \quad \tilde{\mathbf{B}}^{\rm rad} \;=\; \tilde{\mathbf{B}}^{\rm rad}_{+}+\tilde{\mathbf{B}}^{\rm rad}_{-}, \quad \big\langle\tilde{\mathbf{S}}\cdot\hat{\mathbf{n}}\big\rangle_\eta = \big\langle\tilde{\mathbf{S}}_{+}\cdot\hat{\mathbf{n}}\big\rangle_\eta+\big\langle\tilde{\mathbf{S}}_{-}\cdot\hat{\mathbf{n}}\big\rangle_\eta+\big\langle\text{cross}\big\rangle_\eta \;=\; 0. \tag{C.6}$$

Physically: a stationary bound state cannot feed a net outward radiative flux at infinity in the conformal frame; its fields are reactive/evanescent (near–field) with zero net energy transport per cycle. By (C.4), this implies $\langle P\rangle = 0$ in the physical metric as well.

Dipole check (selection rule form). In the conformal frame, the leading radiative channel is dipole radiation with power $\tilde{P}_{\rm dip} \propto \big|\frac{d^2\tilde{\mathbf{d}}}{d\eta^2}\big|^2$, where $\tilde{\mathbf{d}}(\eta) = \int \boldsymbol{\chi}\,\tilde{\rho}\,d^3\chi$. For *stationary* bound states the source has definite parity and a fixed azimuthal structure (over a cycle), so the net dipole channel averages to zero; transitions (e.g. $2p \to 1s$) occur only when the source acquires the appropriate oscillatory component at the transition frequency, reproducing the usual selection rules. Hence $\langle\tilde{P}_{\rm dip}\rangle_\eta = 0$ in stationary states.

C.4 Local criterion via proper acceleration

A complementary local statement uses the covariant Larmor scalar. Let $u^\mu = dx^\mu/d\tau$ be the four–velocity and $a^\mu = u^\nu\nabla_\nu u^\mu$ the *proper* four–acceleration in the physical metric $g_{\mu\nu} = A^2\eta_{\mu\nu}$. The radiative power measured in the comoving frame is proportional to the invariant

$$\mathcal{P} \;\propto\; q^2\, a^\mu a_\mu\,, \tag{C.7}$$

so worldlines with $a^\mu a_\mu = 0$ do not radiate locally.[2] In the conformal metric (C.1), geodesics satisfy $a^\mu = 0$. The VBT construction takes the *fabric–frame* motion to be uniform between turning regions (piecewise geodesic in $(\eta, \boldsymbol{\chi})$), so that $a^\mu a_\mu = 0$ except where the binding potential reverses the motion. The global statement (C.6) then guarantees that the cycle–averaged power still vanishes: the transient local accelerations at turning regions do not produce a net outward $1/R$ flux when the full standing–wave source is taken into account.

C.5 Conclusion

Maxwell's conformal behavior reduces the radiation question to a flat–space calculation in conformal coordinates. Stationary bound states correspond to standing–wave sources, which carry no net Poynting flux through a distant sphere per cycle; by conformal scaling, the physical radiated power also averages to zero. Equivalently, the covariant Larmor scalar $a^\mu a_\mu$ vanishes along the uniform fabric–frame segments of the motion, and the remaining turning–region contributions cancel at the level of the far–field $1/R$ terms. Therefore, stationary VBT orbitals are *non–radiating*.

D Lagrangian Formulation for Electromagnetism in the Breathing Vacuum

For completeness, we recall the standard electromagnetic Lagrangian density :

$$\mathcal{L}_{\rm EM} = -\frac{1}{4} F_{\mu\nu} F^{\mu\nu} - J_\mu A^\mu, \tag{D.1}$$

where $F_{\mu\nu} = \partial_\mu A_\nu - \partial_\nu A_\mu$ is the field strength tensor and J_μ is the 4-current density. This conventional formulation provides the baseline against which VBT modifications may be compared, without invoking additional assumptions from quantum electrodynamics [36].

A concise action for the transverse degrees of freedom of the vacuum fabric is

$$S_{\rm EM} = \int d^4x \; \frac{\rho_v}{2} \left[\frac{1}{c^2} (\partial_t \boldsymbol{\xi}_\perp)^2 - (\nabla \boldsymbol{\xi}_\perp)^2 \right], \tag{D.2}$$

where $c^2 = \kappa_v / \rho_v$ as in Section 8. Introducing the vector potential

$$\mathbf{A} \equiv \Lambda \, \partial_t \boldsymbol{\xi}_\perp, \tag{D.3}$$

and defining $A_\mu = (\phi/c, \, \mathbf{A})$, the action becomes

$$S_{\rm EM} = -\frac{1}{4\mu_0} \int d^4x \; F_{\mu\nu} F^{\mu\nu}, \tag{D.4}$$

with $F_{\mu\nu} = \partial_\mu A_\nu - \partial_\nu A_\mu$ and $\mu_0^{-1} = \Lambda^2 \rho_v c^2$. Varying with respect to A_μ yields the source-free Maxwell equations. Coupling to matter is introduced via

$$S_{\rm int} = \int d^4x \; J^\mu A_\mu, \tag{D.5}$$

which enforces charge conservation $\partial_\mu J^\mu = 0$.

[2] In flat space this reduces to the Liénard formula; the generalization to curved spacetimes keeps the same scalar $a^\mu a_\mu$ in the local limit.

D.1 Charge as a Topological Defect in the Vacuum Fabric

In VBT, electric charge corresponds to a topological winding of an internal $U(1)$ order parameter $\theta_{U(1)}(\mathbf{x})$, not of the global Planck carrier. The carrier $\Phi_P(t)$ remains strictly synchronized everywhere. A 2π winding in $\theta_{U(1)}$ produces quantized flux, consistent with Gauss's law. Thus charge is a defect in the vacuum's internal orientation, while the underlying breathing oscillation is untouched.

D.2 Remarks

This picture unifies:

- **Elastic wave physics** of the vacuum fabric with the **field theory** of electromagnetism.
- **Charge conservation** with **topological invariance** of phase winding.
- **Gauge symmetry** with the freedom to redefine the carrier phase without changing measurable fields.

At Planck resolution, both the breathing (longitudinal) and shear (transverse) modes coexist, but only the shear modes survive as propagating disturbances at low frequency, giving rise to photons.

E Lagrangian Formulation for Gravity

The standard Einstein–Hilbert Lagrangian [4, 41] is

$$\mathcal{L}_{\mathrm{GR}} = \frac{1}{16\pi G} R\sqrt{-g} + \mathcal{L}_{\mathrm{matter}}, \tag{E.1}$$

where R is the Ricci scalar and g the determinant of the metric tensor. In VBT, the same form can be recovered by interpreting curvature as local suppression of the breathing amplitude A_{mean}, linking the gravitational action to the Planck-scale substrate.The longitudinal (breathing) degree of freedom of the vacuum fabric is encoded in the scalar field $\chi(t, \mathbf{x})$ representing the local fractional dilation of the metric scale factor $\Omega(t, \mathbf{x})$:

$$\Omega(t, \mathbf{x}) = 1 + \varepsilon\, \chi(t, \mathbf{x}), \tag{E.2}$$

with $\varepsilon \ll 1$ in the weak-field regime.

A minimal action for χ is

$$S_{\mathrm{grav}} = \frac{\rho_v}{2} \int d^4x \left[\frac{1}{c^2} (\partial_t \chi)^2 - (\nabla \chi)^2 \right], \tag{E.3}$$

where ρ_v is the effective vacuum mass density. This is a scalar wave equation with wave speed c for the longitudinal mode.

E.1 Coupling to Matter

Matter with mass density $\rho_m(\mathbf{x}, t)$ couples to the breathing mode via the interaction term

$$S_{\mathrm{int}} = -\frac{\rho_v}{c^2} \int d^4x\ \Phi_g(\mathbf{x}, t)\, \rho_m(\mathbf{x}, t), \tag{E.4}$$

where Φ_g is identified as the *mean-field gravitational potential*:

$$\Phi_g(\mathbf{x}, t) \equiv \frac{c^2}{2}\,\chi(\mathbf{x}, t). \tag{E.5}$$

Variation of $S_{\text{grav}} + S_{\text{int}}$ with respect to χ yields

$$\frac{1}{c^2}\partial_t^2\chi - \nabla^2\chi = \frac{\rho_m}{\rho_v}. \tag{E.6}$$

E.2 Newtonian Limit

In the static, weak-field limit ($\partial_t\chi \approx 0$) this reduces to

$$\nabla^2\Phi_g = 4\pi G\,\rho_m, \tag{E.7}$$

with G fixed by the ratio ρ_v/c^2:

$$G \equiv \frac{c^4}{8\pi\rho_v}. \tag{E.8}$$

Thus Newton's law is recovered as the time-averaged limit of the breathing mode dynamics.

E.3 Mass as a Localized Amplitude Defect

In VBT, mass is modeled as a localized suppression of the vacuum breathing amplitude. This defect shifts the cycle-averaged midpoint A_{mean} downward, sourcing the effective potential Φ that appears in the weak-field metric. The Planck-frequency carrier remains globally synchronized. What gravitates is not a phase offset but the depth of amplitude suppression. This reproduces the Gauss-law form $\nabla^2\Phi = 4\pi G\rho$ while maintaining a universal carrier phase.

E.4 Remarks

This construction places:

- **Gravity** as the longitudinal oscillation mode of the vacuum fabric.
- **Mass** as a conserved topological phase defect in that mode.
- The **Newtonian limit** as the static solution of the scalar wave equation.
- **GR corrections** as higher-order terms when ε is not small.

At the Planck scale, transverse (EM) and longitudinal (gravitation) modes are simply orthogonal oscillations of the same underlying medium.

F Weak–Field Derivation of Gravity from Amplitude Suppression

Starting from the weak-field metric of Eq. 58 reproduces the standard form of General Relativity [4, 41]. The effective potential Φ satisfies Poisson's equation $\nabla^2\Phi = 4\pi G\rho$, where G is the Newtonian constant [37]. Observable consequences include gravitational redshift, light bending, and radar time delay, all matching the predictions of GR while being interpreted within VBT as consequences of suppressed breathing amplitude.

We derive Newtonian acceleration, gravitational redshift, and light bending starting from the metric ansatz of Eq. (F.1).

$$ds^2 = A(x)^2c^2dt^2 - A(x)^{-2}dx^2, \qquad A(x) = e^{\Phi(x)/c^2}. \tag{F.1}$$

F.1 Christoffel symbols in the weak field

For weak potentials, $A \approx 1 + \Phi/c^2$. Expanding to first order in Φ/c^2, the metric components are

$$g_{00} = \left(1 + \frac{2\Phi}{c^2}\right) c^2, \qquad g_{ij} = -\left(1 - \frac{2\Phi}{c^2}\right) \delta_{ij}.$$

This matches the isotropic weak-field form of the Schwarzschild metric.

The nonvanishing Christoffel symbols to first order are

$$\Gamma^i{}_{00} \approx +\frac{1}{c^2}\,\partial_i\Phi, \tag{F.2}$$

$$\Gamma^0{}_{0i} \approx \frac{1}{c^2}\,\partial_i\Phi, \tag{F.3}$$

$$\Gamma^i{}_{jk} \approx \frac{1}{c^2}\left(\delta_{jk}\,\partial_i\Phi - \delta_{ij}\,\partial_k\Phi - \delta_{ik}\,\partial_j\Phi\right). \tag{F.4}$$

F.2 Equation of motion for slow bodies

The spatial geodesic equation is

$$\frac{d^2x^i}{d\tau^2} + \Gamma^i{}_{00}\left(\frac{dt}{d\tau}\right)^2 \approx 0.$$

Since for slow motion $dt/d\tau \approx 1$, we obtain

$$\frac{d^2x^i}{dt^2} \;\approx\; -\,\partial_i\Phi, \tag{F.5}$$

i.e. the Newtonian acceleration law.

F.3 Frequency shift

The proper time of a stationary clock satisfies

$$d\tau = \sqrt{g_{00}}\,dt \approx \left(1 + \frac{\Phi}{c^2}\right) dt,$$

so the frequency ratio between two positions is

$$\frac{\nu_{\text{obs}}}{\nu_{\text{em}}} \approx 1 + \frac{\Phi_{\text{obs}} - \Phi_{\text{em}}}{c^2}, \tag{F.6}$$

the gravitational redshift formula.

F.4 Light rays and index of refraction

For null curves ($ds^2 = 0$) in the spatially isotropic form, the effective optical metric is

$$d\ell^2 = A(\mathbf{x})^{-4}\,d\mathbf{x}^2.$$

This is equivalent to propagation in a medium with refractive index

$$n(\mathbf{x}) = A(\mathbf{x})^{-2} \approx 1 - \frac{2\Phi(\mathbf{x})}{c^2}.$$

The deflection angle for a light ray grazing a mass M at impact parameter b is

$$\Delta\theta \;=\; \frac{4GM}{c^2 b}, \tag{F.7}$$

recovering the full general-relativistic result (time scaling alone would give half this value).

F.5 Summary

Starting from a uniform carrier phase and amplitude suppression $A(\mathbf{x}) = e^{\Phi/c^2}$, we recover:

- Newtonian acceleration in the weak field;
- Gravitational redshift and time dilation;
- Light bending and Shapiro delay with the correct GR coefficient.

Thus, the VBT interpretation (gravity as amplitude suppression) is mathematically consistent with classical tests of general relativity.

G Vacuum birefringence

In strong external fields the vacuum acquires effective nonlinearities described by the Heisenberg–Euler Lagrangian,

$$\mathcal{L}_{\rm HE} = \tfrac{1}{2}\big(\mathbf{E}^2 - \mathbf{B}^2\big) + \frac{2\alpha^2}{45 m_e^4}\Big[\big(\mathbf{E}^2 - \mathbf{B}^2\big)^2 + 7\big(\mathbf{E}\cdot\mathbf{B}\big)^2\Big]. \tag{G.1}$$

For a probe wave propagating perpendicular to a static magnetic field B, the refractive indices for polarizations parallel/perpendicular to B are

$$n_\parallel - 1 = \frac{7\alpha}{90\pi}\left(\frac{B}{B_c}\right)^2, \tag{G.2}$$

$$n_\perp - 1 = \frac{4\alpha}{90\pi}\left(\frac{B}{B_c}\right)^2, \tag{G.3}$$

with

$$B_c = \frac{m_e^2 c^3}{e\hbar} \simeq 4.4 \times 10^9\ \mathrm{T}. \tag{G.4}$$

The birefringence signal is therefore

$$\Delta n_{\rm QED} = n_\parallel - n_\perp = \frac{3\alpha}{90\pi}\left(\frac{B}{B_c}\right)^2. \tag{G.5}$$

G.1 VBT expectation.

Within the breathing framework, Maxwell's equations remain conformally invariant, so the leading nonlinearity is unchanged. Any VBT correction appears as a fractional modification of the Heisenberg–Euler coefficients,

$$\Delta n_{\rm VBT} = \Delta n_{\rm QED}\,(1 + \xi), \qquad \xi = \mathcal{O}(\varepsilon^2), \tag{G.6}$$

which vanishes as the breathing amplitude $\varepsilon \to 0$. Vacuum birefringence therefore acts as a null test for VBT-specific corrections.

G.2 Laboratory bound.

At $B \simeq 2.5\,\mathrm{T}$, QED predicts

$$\Delta n_{\mathrm{QED}} \approx 2.5 \times 10^{-23}. \tag{G.7}$$

PVLAS reports

$$\Delta n = (12 \pm 17) \times 10^{-23} \qquad (B = 2.5\,\mathrm{T}), \tag{G.8}$$

consistent with the prediction within sensitivity [38, 51]. This constrains deviations to

$$|\xi| \lesssim 7 \;\; (1\sigma), \qquad |\xi| \lesssim 20 \;\; (3\sigma). \tag{G.9}$$

G.3 Astrophysical evidence.

Optical polarimetry of neutron star RX J1856.5-3754 reported a linear polarization degree of ∼16, supporting the existence of vacuum birefringence in the strong-field regime [52]. Recent X-ray polarimetric observations of magnetars by IXPE—including the first measurements from 4U 0142+61 and 1E 1841-045—show strong, energy-dependent polarization patterns that are consistent with QED-induced birefringence and mode conversion effects [33, 34].

G.4 Summary.

VBT predicts the same birefringence signal as QED at leading order. Present laboratory and astrophysical observations are consistent, while a future laboratory detection of Δn at the QED level would immediately constrain any breathing-induced correction ξ to $\ll 1$.

H Simulation validation

To validate the analytic radial probability densities, we generated synthetic trajectories using the inverse-CDF method. A uniform random sequence $u \in [0, 1]$ was mapped to radii r by inverting the cumulative distribution $F(r) = \int_0^r P(r')\,dr'$ of the target hydrogenic state. By stepping through this sequence at fixed angular increments we obtain time series $r(t)$ whose histograms can be compared directly to the analytic distributions. This procedure reproduces the correct weighting by sampling design and is used purely as a numerical validation tool, not as an independent derivation.

For completeness we present additional checks for the $2s$ and $2p$ states that were omitted from the main text for brevity.

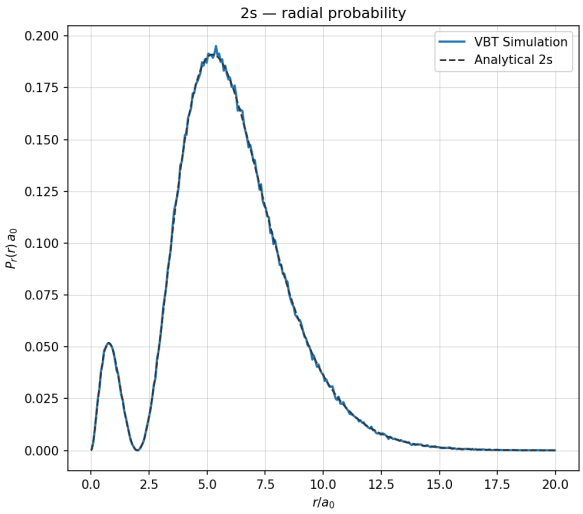

(a) $2s$ radial distribution

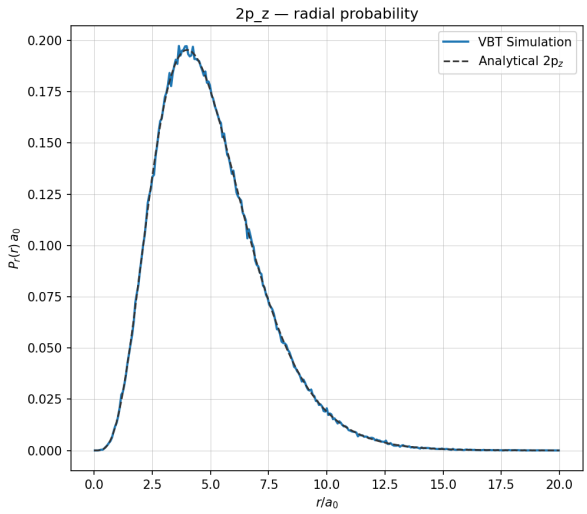

(b) $2p$ radial distribution

Figure 18: **Validation of the $2s$ and $2p$ radial distributions.** Histograms of radii $r(t)$ from inverse-CDF validation compared with the analytic densities. Both cases show L_1 error $\lesssim 10^{-2}$, confirming that the sampling method reproduces the analytic distributions.

Summary. These results demonstrate that the inverse-CDF validation produces trajectories whose histograms agree with the analytic radial PDFs for the $2s$ and $2p$ states. They serve as validation of the analytic derivation presented in Sec. 4.4, not as an independent assumption.

References

[1] Max Planck. On the law of distribution of energy in the normal spectrum. *Annalen der Physik*, 4:553–563, 1901.

[2] Niels Bohr. On the constitution of atoms and molecules. *Philosophical Magazine*, 26(151):1–25, 1913.

[3] Erwin Schrödinger. Quantisierung als Eigenwertproblem. *Annalen der Physik*, 79:361–376, 1926.

[4] Albert Einstein. Die grundlage der allgemeinen relativitätstheorie. *Annalen der Physik*, 49:769–822, 1916.

[5] Edwin Hubble. A relation between distance and radial velocity among extra-galactic nebulae. *Proceedings of the National Academy of Sciences*, 15(3):168–173, 1929.

[6] Planck Collaboration. Planck 2018 results. vi. cosmological parameters. *Astronomy & Astrophysics*, 641:A6, 2020.

[7] David L. Poole. Testing the temporal structure of single-photon emission with trapped ions, 2025. Revision 2.

[8] David Izabel. Analogy of space time as an un-elastic medium – can we establish a thermal expansion coefficient of space from the cosmological constant λ? *arXiv preprint*, 2023. arXiv:2310.01005.

[9] David Izabel. Analogy of space-time as an elastic medium, estimation creep coefficient of space from mond theory, gravitational lensing and via time data from the gps effect. *International Journal of Modern Physics D*, 2024. arXiv:2412.13277.

[10] David Izabel. Analogy of space-time as an elastic medium – state of the art and perspectives on the knowledge of time. *preprint*, 2025. Preprints.org, doi:10.20944/preprints202508.1443.v1.

[11] David L. Poole. Vacuum breathing theory: A deterministic framework for atomic structure and cosmology, 2025. First public preprint, Rev.1, 10.5281/zenodo.17050452.

[12] Louis de Broglie. *Recherches sur la théorie des quanta*. PhD thesis, Université de Paris, 1924.

[13] E. Madelung. Quantentheorie in hydrodynamischer form. *Zeitschrift für Physik*, 40:322–326, 1927.

[14] Werner Heisenberg. Über den anschaulichen inhalt der quantentheoretischen kinematik und mechanik. *Zeitschrift für Physik*, 43:172–198, 1927.

[15] H. P. Robertson. The uncertainty principle. *Physical Review*, 34:163–164, 1929.

[16] P. A. M. Dirac. The quantum theory of the electron. *Proceedings of the Royal Society A*, 117:610–624, 1928.

[17] Hans A. Bethe and Edwin E. Salpeter. *Quantum Mechanics of One- and Two-Electron Atoms*. Springer, 1957.

[18] S. P. Goldman and G. W. F. Drake. Relativistic two-photon decay rates in hydrogen-like ions. *Phys. Rev. A*, 24:183–192, 1981.

[19] W. E. Lamb and R. C. Retherford. Fine structure of the hydrogen atom by a microwave method. *Phys. Rev.*, 72:241–243, 1947.

[20] C. Schwob, L. Jozefowski, B. de Beauvoir, L. Hilico, F. Nez, L. Julien, and F. Biraben. Optical frequency measurement of the $2s - 12d$ transitions in hydrogen and deuterium: Rydberg constant and lamb shift determinations. *Phys. Rev. Lett.*, 82:4960–4963, 1999.

[21] K. S. Novoselov et al. Two-dimensional gas of massless dirac fermions in graphene. *Nature*, 438:197–200, 2005.

[22] Luna Y. Liu, Steffi Y. Woo, Jinyuan Wu, Bowen Hou, Cong Su, Diana Y. Qiu, et al. Direct observation of massless excitons and linear exciton dispersion in monolayer hexagonal boron nitride. *arXiv preprint arXiv:2502.20454*, 2025. measured linear exciton branch due to long-range exchange;.

[23] Alessandro Nicolaou, Kari Ruotsalainen, Laura Susana, Victor Porée, Luiz Galvao Tizei, Jaakko Koskelo, et al. Direct measurement of the longitudinal exciton dispersion in hbn by resonant inelastic x-ray scattering. *Physical Review B*, 112:085207, 2025.

[24] E. H. Hauge and J. A. Støvneng. Tunneling times: a critical review. *Reviews of Modern Physics*, 61(4):917–936, 1989.

[25] A. M. Steinberg, P. G. Kwiat, and R. Y. Chiao. Measurement of the single-photon tunneling time. *Physical Review Letters*, 71(5):708–711, 1993.

[26] K. von Klitzing, G. Dorda, and M. Pepper. New method for high-accuracy determination of the fine-structure constant based on quantized hall resistance. *Physical Review Letters*, 45(6):494–497, 1980.

[27] K. S. Novoselov, A. K. Geim, S. V. Morozov, D. Jiang, M. I. Katsnelson, I. V. Grigorieva, S. V. Dubonos, and A. A. Firsov. Two-dimensional gas of massless dirac fermions in graphene. *Nature*, 438:197–200, 2005.

[28] Massimiliano Rossi, Andrei Militaru, Nicola Carlon Zambon, Andreu Riera-Campeny, Oriol Romero-Isart, Martin Frimmer, and Lukas Novotny. Quantum delocalization of a levitated nanoparticle. *Physical Review Letters*, 135(8):h3601, 2025.

[29] S. L. Adler. Photon splitting and photon dispersion in a strong magnetic field. *Annals of Physics*, 67:599–647, 1971.

[30] E. Zavattini et al. Experimental observation of optical rotation generated in vacuum by a magnetic field. *Physical Review Letters*, 96:110406, 2006.

[31] A. Cadène et al. Vacuum magnetic birefringence experiment. *European Physical Journal D*, 68:16, 2014.

[32] H. von Helmholtz. Über integrale der hydrodynamischen gleichungen, welche den wirbelbewegungen entsprechen. *Journal für die reine und angewandte Mathematik*, 55:25–55, 1858.

[33] Dong Lai et al. Ixpe detection of polarized x-rays from magnetars and photon mode conversion at qed vacuum resonance. *Proceedings of the National Academy of Sciences*, 120:e2301683120, 2023.

[34] Michela Rigoselli et al. Ixpe detection of highly polarized x-rays from the magnetar 1e 1841-045. *arXiv preprint*, 2024.

[35] John David Jackson. *Classical Electrodynamics*. Wiley, 3 edition, 1998.

[36] Claude Cohen-Tannoudji, Jacques Dupont-Roc, and Gilbert Grynberg. *Atom–Photon Interactions: Basic Processes and Applications*. Wiley, 1992.

[37] Particle Data Group. Review of particle physics. *Progress of Theoretical and Experimental Physics*, 2024(8):083C01, 2024.

[38] R. Battesti and C. Rizzo. Magnetic and electric properties of quantum vacuum. *Rep. Prog. Phys.*, 76:016401, 2013.

[39] Gerald V. Dunne. The heisenberg–euler effective action: 75 years on. *arXiv e-prints*, 2012.

[40] Elda Guzman-Herrera and Nora Breton. Euler–heisenberg waves propagating in a magnetic background. *European Physical Journal C*, 81(115), 2021.

[41] James B. Hartle. *Gravity: An Introduction to Einstein's General Relativity*. Addison-Wesley, 2003.

[42] C. M. Will. The confrontation between general relativity and experiment. *Living Reviews in Relativity*, 17(4), 2014.

[43] C. Alcock et al. The macho project: Microlensing results from 5.7 years of lmc observations. *Astrophysical Journal*, 542:281–307, 2000.

[44] P. Tisserand et al. Limits on the macho content of the galactic halo from the eros-2 survey. *Astronomy and Astrophysics*, 469:387–404, 2007.

[45] Michael Faraday. On the rotation of the plane of polarization of light by magnetic forces. *Philosophical Transactions of the Royal Society of London*, 136:1–20, 1846.

[46] John Kerr. A new relation between electricity and light: Dielectric media birefringent in the presence of an electric field. *Philosophical Magazine*, 50:337–348, 1875.

[47] H. B. G. Casimir. On the attraction between two perfectly conducting plates. *Proceedings of the Koninklijke Nederlandse Akademie van Wetenschappen*, 51:793–795, 1948.

[48] Steve K. Lamoreaux. Demonstration of the casimir force in the 0.6 to 6 μm range. *Physical Review Letters*, 78(1):5–8, 1997.

[49] Umar Mohideen and Anushree Roy. Precision measurement of the casimir force from 0.1 to 0.9 μm. *Physical Review Letters*, 81(21):4549–4552, 1998.

[50] NIST Atomic Spectra Database. Nist atomic spectra database (levels, transition probabilities). https://physics.nist.gov/asd. Accessed 2025.

[51] F. Della Valle and others (PVLAS Collaboration). First results from the new pvlas apparatus: A new limit on vacuum magnetic birefringence. *Phys. Rev. D*, 90:092003, 2014.

[52] R. P. Mignani et al. Evidence for vacuum birefringence from the first optical-polarimetry measurement of the isolated neutron star rx j1856.5–3754. *Monthly Notices of the Royal Astronomical Society*, 465:492–500, 2017.